AFRL-AFOSR-VA-TR-2020-0055

Uncovering and controlling the mechanisms of surface chemical and electrochemical stability on perovskite oxides

Bilge Yildiz
MASSACHUSETTS INSTITUTE OF TECHNOLOGY

01/10/2020
Final Report

Air Force Research Laboratory
AF Office Of Scientific Research (AFOSR)/ RTB1
Arlington, Virginia 22203
Air Force Materiel Command

REPORT DOCUMENTATION PAGE

Form Approved
OMB No. 0704-0188

1. REPORT DATE *(DD-MM-YYYY)*	2. REPORT TYPE	3. DATES COVERED *(From - To)*
18-06-2020	Final Performance	30 Sep 2016 to 29 Sep 2019

4. TITLE AND SUBTITLE
Uncovering and controlling the mechanisms of surface chemical and electrochemical stability on perovskite oxides

5a. CONTRACT NUMBER

5b. GRANT NUMBER
FA9550-16-1-0427

5c. PROGRAM ELEMENT NUMBER
61102F

6. AUTHOR(S)
Bilge Yildiz

5d. PROJECT NUMBER

5e. TASK NUMBER

5f. WORK UNIT NUMBER

7. PERFORMING ORGANIZATION NAME(S) AND ADDRESS(ES)
MASSACHUSETTS INSTITUTE OF TECHNOLOGY
77 MASSACHUSETTS AVE
CAMBRIDGE, MA 02139-4301 US

8. PERFORMING ORGANIZATION REPORT NUMBER

9. SPONSORING/MONITORING AGENCY NAME(S) AND ADDRESS(ES)
AF Office of Scientific Research
875 N. Randolph St. Room 3112
Arlington, VA 22203

10. SPONSOR/MONITOR'S ACRONYM(S)
AFRL/AFOSR RTB1

11. SPONSOR/MONITOR'S REPORT NUMBER(S)
AFRL-AFOSR-VA-TR-2020-0055

12. DISTRIBUTION/AVAILABILITY STATEMENT
A DISTRIBUTION UNLIMITED: PB Public Release

13. SUPPLEMENTARY NOTES

14. ABSTRACT
Understanding the effects of surface composition, gas environment, and high temperatures on the oxygen exchange kinetics of functional perovskite oxides is essential to ensure high long-term stability for their applications in energy technology and electronics. In this project, we have focused on the surface processes underlying one of their main degradation mechanisms: high-temperature surface segregation of dopants, leading to the formation inactive surface phase. Based on the understanding of the segregation mechanism, we have also investigated a way to remove such surface degradation by applying electrical polarization.

15. SUBJECT TERMS
perovskite, charge transfer, surface charge, Auger electron, Auger electron spectroscopy

16. SECURITY CLASSIFICATION OF:			17. LIMITATION OF ABSTRACT	18. NUMBER OF PAGES	19a. NAME OF RESPONSIBLE PERSON
a. REPORT	b. ABSTRACT	c. THIS PAGE			SAYIR, ALI
Unclassified	Unclassified	Unclassified	UU		19b. TELEPHONE NUMBER *(Include area code)* 703-696-7236

Standard Form 298 (Rev. 8/98)
Prescribed by ANSI Std. Z39.18

Final Report for: Uncovering and controlling the mechanisms of surface chemical and electrochemical stability on perovskite oxides-

Modifying the surface stability of doped $LaMnO_3$ by electrical polarization and metal deposition

Dongha Kim, Roland Bliem, Bilge Yildiz, MIT

Abstract

Understanding the effects of surface composition, gas environment, and high temperatures on the oxygen exchange kinetics of functional perovskite oxides is essential to ensure high long-term stability for their applications in energy technology and electronics. In this project, we have focused on the surface processes underlying one of their main degradation mechanisms: high-temperature surface segregation of dopants, leading to the formation inactive surface phase. Based on the understanding of the segregation mechanism, we have also investigated a way to remove such surface degradation by applying electrical polarization.

During the first two years of the project, we investigated the surface properties of doped $LaMnO_3$ as a model system to study how the surface stability of functional perovskite oxides is affected by polarization and doping of the surface layer; 1) The effect of electrochemical polarization of $La_{0.8}Ba_{0.2}MnO_3$ (LBM) $La_{0.8}Sr_{0.2}MnO_3$ (LSM), and $La_{0.8}Ca_{0.2}MnO_3$ (LCM) thin films, 2) as well as of the deposition of Hf on $La_{0.8}Sr_{0.2}MnO_3$ on their segregation behavior have been performed successfully. 3) Measurements of the structure of low-index LSM surfaces and of the segregated SrO_x phase helped us better understand the surface processes in atomic scale. We could also develop a theoretical background on how the degradation proceeds under different oxygen chemical potentials on each perovskite compound, LBM, LSM, and LCM. During the last year, based on all these findings and knowledges, 4) we were able to develop a way to remove the dopant segregation on each compound by inducing a targeted surface reaction with electrical polarization. Below is a brief summary of our results following the order of the above numberings:

1) The effect of polarization on dopant segregation behavior of doped $LaMnO_3$:

The effects of electrochemical polarization are studied on Ca-, Sr-, and Ba-doped $LaMnO_3$. Applying polarization changes the oxygen chemical potential in the electrode thin films, and thus modifies the oxygen vacancy concentration. The three dopants of choice (Ca, Sr, and Ba) carry the same charge but have different ionic sizes, resulting in an equivalent response to changes in the defect distribution but different elastic energies within the lattice. This selection thus allows assessing the role the two main driving forces of segregation, both of which change as a function of oxygen content: (i) the electrostatic attraction of the dopant cation to the surface, which is enriched in charged oxygen vacancies (ii) the elastic energy created by the size mismatch of the

dopant and the host cation La. Both driving forces result in the precipitation of the dopant to the surface in an oxide form, e.g. SrO_x, by interacting with gaseous oxygen in the environment. Here, we investigate the balance of these two contributions by selectively controlling the elastic energy of dopants and monitoring their segregation using X-ray photoelectron spectroscopy (XPS) and imaging techniques. Polarization is applied using a recently developed approach based on a linear lateral potential gradient across the surface. The investigated voltage ranges from -0.8 V to +0.8 V corresponds to effective oxygen pressures spanning 31 orders of magnitude (from 10^{-16} to 10^{15} atm, according to the Nernst equation). We observe progressive enhancement of Sr and Ba segregation with increasing bias voltage for both polarities, whereas Ca segregation only increases for cathodic polarization. This observation is interpreted as a transition between the electrostatically and elastically dominated regimes for Ba and Sr. In contrast, Ca segregation exclusively responds to changes in the electrostatic energy due to the small size mismatch between Ca and the host A-site cation, La^{3+}. The present study provides quantitative insights into how the elastic energy, manifested by lattice parameter and cation size, and the electrostatic energy, manifested by charged defect concentration and distribution, determine the extent of segregation for a given polarization and atmosphere relevant to the operating conditions of perovskite oxide materials. With a collaborative work with Dr. Franziska Hess, a postdoctoral associate in our group, we could also find representative defect reactions that explain the dopant segregation under both cathodic and anodic polarizations. We have submitted a manuscript with the above results and it is currently under review.

2) The effect of surface metal doping on the dopant segregation behavior of LSM:

In addition to the polarization-dependence of segregation, the response of the surface stability to surface metal doping has been studied. The deposition of metals is expected to modify the equilibrium surface oxygen vacancy concentration, thus modifying the electrostatic driving force of segregation. Here, we study the effect of doping the surface of LSM thin films with Hf, which shows a high affinity to oxygen and form a difficult-to-reduce oxide. Using ambient-pressure XPS at 450°C and 550°C in 1 mTorr O_2, we observe lower segregation when the surface of LSM thin film is doped with Hf. This behavior is attributed to the decrease in equilibrium oxygen vacancy concentration at the surface resulting from incorporation of Hf into the surface of LSM. The results will be submitted for publication in the near future.

3) Structural properties of LSM surfaces and the surface SrO_x precipitates:

Structural properties of LSM surface and SrO_x precipitates have been investigated using scanning tunneling microscopy (STM), low-energy electron diffraction (LEED), and extended X-ray absorption fine structure (EXAFS). While the STM study focuses on the properties of ideal $La_{0.8}Sr_{0.2}MnO_3$ (100) and (110) surfaces, EXAFS is employed to investigate the structural changes occurring with Sr enrichment and the formation of SrO_x. STM and LEED results indicate square and rectangular surface unit cells for LSM (001) and (110) surfaces, respectively. EXAFS results on LSM samples exhibiting different intensities of segregation are dominated by the signature peaks of the bulk perovskite LSM structure. At elevated temperature the emergence of a weak shoulder

of the Sr-Mn peak at slightly higher bond distances is observed, indicating the formation of a new species.

4) Reversible dopant segregation on doped $LaMnO_3$ by electrical polarization:

Lastly, reversibility of dopant segregation is investigated on LCM, LSM, and LBM. Based on the experimental and theoretical results obtained in the part 1), we were able to reverse the dopant segregation of each perovskite compound by inducing appropriate defect reactions under electrical polarization. Anodic polarization on an LCM thin film, which had undergone dopant segregation under cathodic polarization, removed the pre-existing surface insulating dopant oxides (CaO_x) by re-dissolving them into the lattice and the surface oxygen exchange kinetics of LCM regained its original activity in its pristine state ('activation'). This result can be explained by the dismantlement of CaO_x via a surface defect reaction and sequent redissolution of Ca^{2+} into the bulk via the reduced electrostatic energy of dopant (E_{elec}) under anodic polarization. However, there has been no available theory that can explain how the surface precipitates could be dismantled under anodic polarization. Previously proposed defect reaction rather predicts an increased dopant segregation under anodic polarization, which directly contradicts what we observed. In combination with X-ray absorption studies and analysis on the kinetics of reversing dopant segregation, we could propose a theory that can explain the activation under anodic polarizations: anodic polarization oxidized LCM surface and new unit-cells are created at the surface of LCM by incorporating Ca and O from CaO_x into their A- and O-site, respectively. The results will be submitted for publication in the near future.

Introduction

Perovskite oxides (ABO_3) are considered key players in clean energy conversion applications, including in solid oxide fuel cells (SOFCs) [1-6], gas separation membranes [7], catalysts for gas conversion/reformation [8] and syngas production [9]. They are also important in advanced electronics, such as memristive switches [10]. While the diffusion and charge exchange processes occurring in the bulk are considered well-known [11], there is a clear lack of understanding regarding surface processes [12], even though they are crucial in the interaction of the material with the reacting species in the environment.

In fuel and electrolysis cells [13], oxygen exchange (incorporation and evolution) reactions are considered a bottleneck constraining their efficiency. The activity for these reactions suffers from long-term degradation occurring under the demanding conditions of such devices, which involve high temperatures from 700°C to 1000°C, oxidizing atmospheres [1,14], such as air or pure oxygen, and cell voltages, which can approach 1 V. It is thus important to resolve surface degradation that occurs under these operation conditions in order to increase the long-term overall efficiency of the cells. Like in most catalytic processes, the operating conditions usually require a compromise due to the conflicting temperature dependence of stability and reaction rates. In La-based mixed

conducting perovskites such as $La_{1-x}Sr_xCoO_3$ (LSC) or doped manganites $La_{1-x}D_xMnO_3$ (D = Ca^{2+}, Sr^{2+}, Ba^{2+}: LCM, LSM, and LBM, respectively), the decrease in reactivity to oxygen exchange reactions proceeds via the segregation and precipitation of aliovalent dopant cations at high temperatures. The formation of an inactive surface oxide phase [15-20] on these materials under operation conditions drastically decreases the initial high activity for the oxygen reduction reaction.

Dopant segregation in doped $LaMnO_3$ and related compounds is influenced by a variety of parameters. Temperature is one important factor, since it changes the equilibrium defect concentrations [21] and is required to overcome the high migration barriers reported for the diffusion of dopants through the cation vacancies ranging from 2.0 eV to 4.0 eV [22-24]. Another parameter that influences dopant segregation is the microstructure of thin film electrodes, such as grain boundaries or dislocations. The lower coordination and availability of sites at grain boundaries aid accelerated diffusion of dopants, thus facilitating segregation. The diffusion coefficient at grain boundaries can exceed the bulk value by several orders of magnitude [25,26]. Moreover, the segregation behavior can be affected by changed defect formation energies in the electrode. For example, controlling surface composition or reducibility has been shown to modify the intensity of segregation by altering essential properties such as the surface oxygen vacancy concentration [27]. The gas environment, in particular the oxygen partial pressure, is certainly among the most important parameters influencing this degradation behavior, as it changes the oxygen stoichiometry of the electrode materials. Conflicting results can be found in literature, reporting either progressive enhancement [28] or decrease [19] of segregation in LSM with decreasing oxygen pressures. The results reported in these two studies, however, are limited to relatively narrow pressure ranges [28] and small number of sampling points [19]. In LSC and related oxides, a broader range of oxygen chemical potentials has been studied using electrochemical polarization [29-31], resulting in an increase in segregation for cathodic polarization of the electrode. The large gap in ionic conductivity between LSC and LSM and its sister compounds [19,32], however, prohibits simply generalizing conclusions for LSC to all types of perovskite cathode materials [33]. On LSM, previous reports on the polarization-dependent behavior [34,35] focus on the activating/deactivating effect of cathodic/anodic current [36-39] and the oxygen exchange for negative voltages [40,41]. No systematic analysis of the role of polarization in the electrostatic and elastic driving forces of segregation in doped $LaMnO_3$ or related compounds, however, has ever been performed.

1) As a first theme of our project, we use electrochemical polarization to systematically control the electrostatic and elastic driving forces of dopant in $LaMnO_3$. Using polarization enabled us to vary the oxygen chemical potential of the film by the Nernst equation, thereby changing each driving force correspondingly. We employ a recently developed cell configuration utilizing a polarization gradient [40] across a thin-film model electrode to access effective oxygen pressures spanning a range from 10^{-16} to 10^{15} atm. By selecting the three dopant cations, Ca, Sr, and Ba, with the same charge (2+) but highly different cation sizes ($R_{Ca} < R_{Sr} < R_{Ba}$), we add an

additional parameter which allows us to probe the effects of the misfit elastic energy created by the dopants' size mismatch with respect to the host cation La^{3+}.

These two variables, the oxygen chemical potential and the dopant cation size, permit us to disentangle the role of the two predominant mechanisms behind segregation of dopant cations on this type of perovskite oxides reported in the literature [19]: minimization of the elastic (E_{ela}) and the electrostatic energy (E_{elec}) of the dopant cation in the perovskite lattice. The elastic contribution originates from the mismatch between the preferred lattice size of the dopant versus the host lattice. The electrostatic energy arises from the attraction of the negatively charged dopants (D^{2+} on a La^{3+} site) to the surface enriched with positively charged oxygen vacancies [19]. For example on the $La_{0.9}Sr_{0.1}MnO_3$ (001) surface, the oxygen vacancy concentration was reported to exceed the bulk value by a factor of approximately 10^6 under typical SOFC operation conditions, and to exhibit a further increase by three orders of magnitude upon decreasing the oxygen pressure to 10^{-15} atm [42]. Similar differences between the surface and bulk oxygen vacancy concentrations can also be found in other perovskite oxides, including $LaCoO_3$, $LaFeO_3$, $LaNiO_3$ [43], and $SrTiO_3$ [44]. The altered bonding environment at the surface affects the formation energy of defects – in this case the formation of oxygen vacancies is facilitated at the surface, which has also been reported for several binary oxides including CeO_2 [45,46], rutile TiO_2 [47], or MnO_2 [48]. Based on the excess of oxygen vacancies at the surface under increasingly reducing conditions, we postulate that E_{elec} increases with a decrease in oxygen pressure (pO_2), and we test this hypothesis in our experiments in this work.

On the other hand, we propose that the elastic energy (E_{ela}) affects dopant cations in the bulk and changes their solubilities within the lattice. The cation radii of the chosen dopants here are not the same as that of the host. Ca^{2+} is smaller than the host cation La^{3+} (by -1.5 %), and Sr^{2+} and Ba^{2+} are larger by +5.9 % and +18.4 %, respectively. Based on this, the relative stabilities of the dopants in the perovskite lattice decrease along the Ca, Sr, Ba series; the reactivity of the dopant to form these precipitates increases with larger dopant size mismatch with respect to the host. We propose that the concomitant formation of dopant oxides at the surface is caused by chemical reactions of the segregated dopant with oxygen from the environment. These reactions can result in the formation of dopant oxide and peroxide, either in the form of particles on the surface [22,49] or monolayers covering the entire surface [17]. We can thus predict the oxygen chemical potential where the formation of these reaction products sets in for the three dopants and show that this onset oxygen chemical potential is correlated with the dopant cation size. In this work, we probe the two segregation mechanisms described above as a function of oxygen chemical potential modulated by electrochemical polarization of doped $LaMnO_3$ electrodes. Using X-ray photoelectron spectroscopy (XPS), secondary electron microscopy (SEM), and atomic force microscopy (AFM), we observe a progressive enhancement of surface segregation under increasing cathodic polarization for all three compounds. This behavior originates from the electrostatic attraction (E_{elec}) of charged dopants to the surface, which is enriched in oxygen vacancies under reducing conditions. Under anodic polarization, segregation is driven by the instability of dopants within the lattice and the reaction with gaseous oxygen in the environment.

The reactivity of dopant cations is enhanced by lattice misfit strain (E_{ela}) of the large dopant cations in the form of an increase in segregation for LBM and LSM under anodic conditions. For LCM which had negligible E_{ela}, Ca segregation is suppressed under a wide range of anodic polarization. Clear differences in the transition point between the elastically and electrostatically dominated regimes demonstrate the balance between these two driving forces and their response to changes in the oxygen chemical potential. Thus, this study provides a systematic analysis of the role of polarization and effective pO_2 in segregation processes on perovskite oxides and advances the understanding of their driving forces in both reducing and oxidizing conditions.

2) Having seen that electrostatic interaction between dopant and oxygen vacancies plays an important role in dopant segregation, we investigated if the electrostatic energy of dopant can be modulated by changing the reducibility of the surface through doping additional metal cation. This alters the oxygen vacancy formation energy and thus the oxygen vacancy concentration at the surface. On $La_{0.8}Sr_{0.2}CoO_3$, this type of modification has been successfully performed using doping of the surface region via metal deposition [50]. The different nature of the low-temperature solid oxide fuel cell electrode material $La_{0.8}Sr_{0.2}CoO_3$ regarding for example ionic conductivity renders a direct comparison to LSM difficult. In the framework of the present report, we investigate the effect of depositing Hf, a metal forming very stable oxides due to their hard-to-reduce nature, on Sr segregation in LSM. As a result, we observe lower segregation when the surface of LSM thin film is doped with Hf. This behavior is attributed to the decrease in equilibrium oxygen vacancy concentration at the surface resulting from incorporation of Hf into the surface of LSM. Thus, we find a clear enhancement in the surface stability of LSM, indicating that the targeted modification of the surface reducibility is an approach that is broadly applicable to stabilize oxide electrode surfaces against the segregation of aliovalent dopants.

3) While research on the cause of Sr segregation and possible strategies to stabilize the surface of LSM have seen substantial progress, the question of the nature of the SrO_x phase and its role in the surface structure of LSM remains an open question. In an additional essential part of the present project, we aim to resolve the atomic-scale properties of LSM surfaces as well as the structure, nucleation, and growth of SrO_x as a result of Sr segregation using surface-sensitive spectroscopy, diffraction, and imaging techniques.

4) As mentioned above, dopant segregation and the resultant formation of insulating phases, e.g. SrO_x, at the surface block the electron transfer and oxygen exchange pathways, thus leading to a severe drop in oxygen exchange kinetics of the electrode [51,52]. One promising way to tackle this problem in SOFC/EC application is removing dopant segregation by operating perovskite oxides in a reversible mode. For example, Zhu *et al.* demonstrated that operating perovskite oxides alternately under SOEC (anodic polarization) and SOFC (cathodic polarization) mode could far improve their stability by removing dopant segregation during SOFC operation [53]. Similarly, a study by Wang *et al*. showed that the surface oxygen exchange rate of $(La_{0.8}Sr_{0.2})_{0.9}MnO_3$ increased by several tens of times under cathodic polarization by removing dopant segregation

induced under anodic one [52], and such passivation and activation were reversible through several cycles [37]. Equation 1 explains how cathodic polarization induces redissolution of Sr into the perovskite phase during oxygen evolution reaction [37,52].

$$V_{La}''' + SrO_{surf} + 2Mn_{Mn}^{X} \rightarrow Sr_{La}' + 2Mn_{Mn}'' + 1/2O_2 \quad (1)$$

Obviously, activation under cathodic polarization (cathodic activation) is effective for the perovskite oxides whose segregation behavior has positive relation with polarization (red solid curve in **Figure 0-1a**) [29,37,54,55]. The amount of insulating dopant species changes reversibly with applied polarization, following the segregation graph (red dashed curve). **Figure 0-1b** illustrates the advantage of employing such perovskite oxides in a reversible operation between SOEC and SOFC. However, many perovskite oxides often show the opposite segregation behavior; increased dopant segregation under cathodic polarization (blue solid curve in **Figure 0-1a**) [54,56-60]. For such materials in their reversible operation, surface degradation is expected to be removed during SOEC mode as described in **Figure 0-1c** (anodic activation). Several groups demonstrated with various perovskite oxides that SOEC operation (anodic polarization) could remove Sr segregation and far improve the stability of the cell during reversible operations [54,56,57,61,62]. Despite a number of experimental evidence, however, the principle of anodic activation has not been successfully explained so far because it directly contradicts the mechanism shown in equation 1. Applying anodic polarization would in principle induce the reverse reaction of equation 1 and even promote dopant oxide formation at the surface [37,63]. As another activation pathway of perovskite oxides, elucidating the principle of anodic activation would be a pivotal milestone for improving the long-term stability of perovskite oxides not only in their SOFC/EC application, but also in other fields where perovskites are subject to a cycle of reducing and oxidizing environments, e.g., solar thermochemical fuel production.

As described in part 1), we observe that LCM thin film shows suppressed dopant segregation under a wide range of anodic polarization (blue solid curve in **Figure 0-1a**). This is because anodic polarization lowers the electrostatic attraction of negatively charged dopant (Ca_{La}') towards a surface by reducing the number of positively charged surface oxygen vacancies. Hinted by the segregation behavior of LCM, we choose LCM as an ideal model system for investigating the possibility of anodic activation as another activation pathway of perovskite oxides. Broad negative segregation behavior observed in LCM would allow us to do mechanistic studies by investigating its anodic activation process in a wide range of defect chemistry.

In this last part of our project, we show that insulating dopant oxide at the surface of LCM thin film can be removed with anodic polarization, which contradicts the conventional mechanism of activation shown in equation 1. Such anodic activation was also observed in LSM. *In-situ* electrochemical impedance spectroscopy (EIS) shows that applying anodic polarization for a short time reactivates the initially degraded surface of LCM by removing dopant oxide at the surface and this process is reversible during several cycles. By investigating the kinetics of activation process in combination with X-ray absorption spectroscopy (XAS), we could propose a new mechanism behind this novel activation process under anodic polarization; a new fresh

perovskite surface is formed during the oxidation of LCM under anodic polarization and the pre-existing insulating dopant oxides at the surface are dissolved into the new lattice during the process.

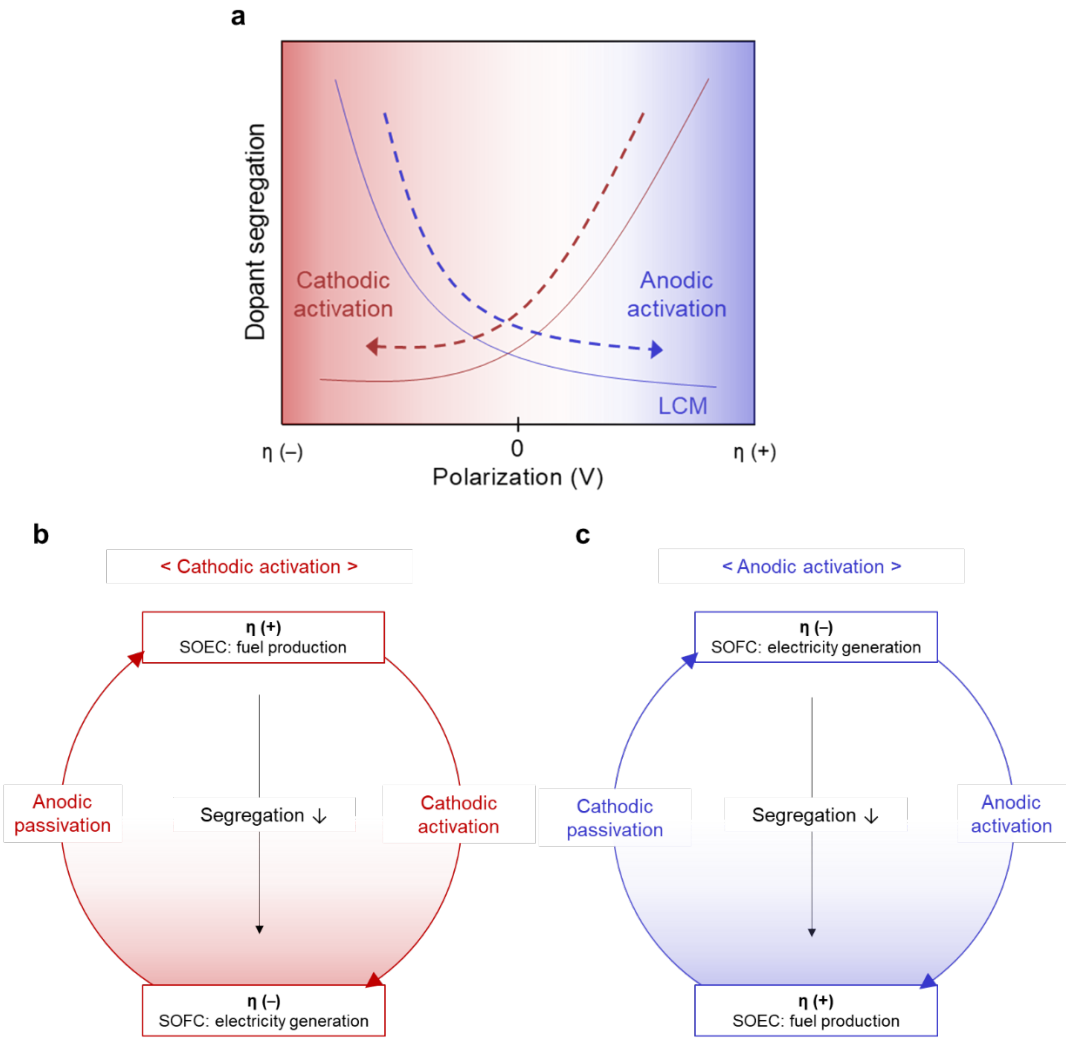

Figure 0-1. Schematics of cathodic and anodic activations during reversible operation between SOFC and SOEC modes. a) Two different segregation behaviors of perovskite oxides with respect to polarization or overpotential (positive relation: red curve, negative relation: blue curve). Corresponding activation on each segregation behavior is indicated as dashed arrow. b) Cathodic activation: SOFC operation (negative overpotential) reactivates perovskite oxide surfaces that were initially degraded under SOEC operation due to dopant segregation. c) Anodic activation: SOEC operation (positive overpotential) reactivates perovskite oxide surface that were initially degraded under SOFC operation due to dopant segregation.

Experimental Methods

1) Lateral polarization of $La_{0.8}D_{0.2}MnO_3$ thin film electrodes

Dense thin-film $La_{0.8}Ba_{0.2}MnO_3$ (LBM), $La_{0.8}Sr_{0.2}MnO_3$ (LSM), and $La_{0.8}Ca_{0.2}MnO_3$ (LCM) electrodes were prepared using pulsed laser deposition (PLD) from each target composition, onto commercial (100)-oriented single crystals of yttria-stabilized zirconia (YSZ, 8 mol% Y_2O_3, purchased from MTI Corp.). The film thickness of approximately 100 nm was measured using a Bruker DXT Stylus profilometer. All the thin film electrodes were deposited at a substrate temperature of 700°C in 0.5 mTorr O_2 and cooled down to room temperature in 500 mTorr O_2. The crystallographic orientation of the films was determined using X-ray diffraction (XRD; Cu Kα radiation, Rigaku Smartlab). Before the growth process, the back and one edge of the YSZ crystals were coated with Pt paint, which establishes a connection between the back side of the electrolyte and a sputter-deposited Pt counter electrode in contact with the perovskite film (**Figure 0-2**). These painted Pt layers, connecting the back, edge, and upper region of the YSZ crystals, are used as a counter electrode in the polarization experiments. This configuration enables us to establish a continuous gradient in polarization in lateral direction on the cathode film surface (see description below). The Pt paint was heated at 700°C in air for 30 min to evaporate the solvent and form a porous Pt layer. After the thin-film growth, electrical contact points were created using sputter deposition of a Ti adhesion layer (10 nm) followed by a Pt contact layer (100 nm). The regions for sputtering were defined by a Kapton mask which covered the films leaving a 2 mm-gap at the side for depositing upper side of the counter electrode. The working electrode was deposited through a 3×7 mm^2-sized rectangular opening of the mask at a distance of 3 mm from the counter electrode. In order to remove pre-existing surface segregate layers, which form on the surface during PLD deposition, the thin-film samples were immersed into a high-purity deionized water for 1 min. This process selectively removed the surface species without significantly compromising the nominal dopant amount in the perovskite phase.

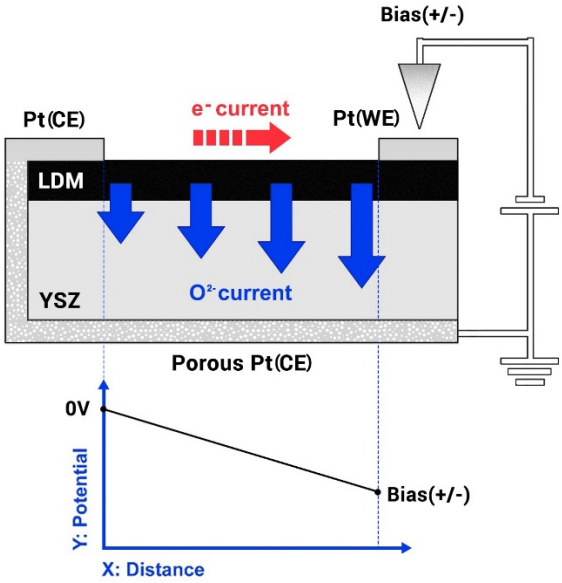

Figure 0-2. Illustration of the experimental setup allowing for applying a continuous polarization gradient across the top electrode surface [40]. The bias voltage applied between the two Pt electrodes leads to a monotonous decrease of the voltage difference applied between the two contacts on the top electrode. The resulting lateral gradient of the oxygen chemical potential is reflected in a gradual variation of the pO_2-dependent surface properties.

The setup for the simultaneous probing of a range of polarization (**Figure 0-2**) is based on the recent design by Huber *et al.* [40]. The sample bias is applied to a Pt contact sputtered onto the electrode film, while the counter electrode (CE), the porous Pt layer on the backside of the YSZ electrolyte, is connected to ground. In contrast to a traditional CE, this model electrode is in electrical contact with a stripe of Pt on the working electrode (WE) film through the thin film electrode. This contact is established by connecting the porous CE to the sputtered Pt contact across one edge of the electrolyte. The sputtered Pt contact point on the WE does not have any contact to the electrolyte or the CE. In this configuration, the thin film electrode responds to a potential difference similar to an Ohmic resistor, resulting in a linear voltage drop across the distance between the two electrodes, shown by Huber *et al.* [40] and confirmed by *in-situ* XPS measurements of LSM under polarization. Thus, applying a bias voltage between the WE and CE (ground) creates a gradient in the electric potential, monotonically changing across the film surface from the full applied voltage at the WE contact to 0 V at the CE contact on the film electrode. As a result, the differences in both the electric potential as well as the oxygen chemical potential between the CE and WE cover a continuous range of values. This novel experimental setup allows us to use one single sample to probe the effect of a large range of bias voltages. This not only saves time, but also eliminates potential experimental variables, such as differences in film thickness, temperature, or pO_2, which can differ slightly between samples and experiments.

In-situ APXPS measurements were performed for cathodically biased LSM at the synchrotron beamline TEMPO at SOLEIL (Paris, France). Considerable levels of the contaminants Cr and MoO_x, however, accumulated on the surface during the measurements, compromising the validity of the acquired data. While the MoO_x species is homogeneously distributed across the sample, the Cr intensity was found to increase close to the (negative) working electrode. The *in-situ* results reported below are only to be considered qualitatively as support for the *ex-situ* observations. Most of the arguments on the lateral polarization experiment are concluded from *ex-situ* experiments, unless noted.

For *ex-situ* measurements, -800 mV, 0 V, and +800 mV were applied to the WE of three separate thin film electrode samples. These potential values correspond to oxygen pressures of 10^{-16}, 1, and 10^{15} atm, respectively. One other sample was reserved as an as-prepared reference sample. The local cation composition at four to five points (±160, ±320, ±480, ±640, -750 mV) between the two electrodes was analyzed by X-ray photoelectron spectroscopy (XPS) using a Physical Electronics Versaprobe II X-ray photoelectron spectrometer equipped with a monochromated Al Kα X-ray source. The distance between each point is constant and corresponds to a potential difference of 160 mV. While applying bias, the films were heated for one hour at 770 °C in an

atmosphere of 1 atm O_2 in a tube furnace. For quantitative analysis, core-level emissions with similar inelastic mean free paths were chosen; these are La 4*d* (λ = 1.7 nm; Mn 3*p* (λ = 1.7 nm); Ba 4*d* (λ = 1.7 nm); Sr 3*d* (λ = 1.6 nm); Ca 2*p* (λ = 1.4 nm) [64]. The angle between the analyzer and the surface plane was set to 45°. Angle-resolved XPS (AR-XPS) was used to analyze the cation composition both in a more surface-sensitive (20° with respect to the surface plane) mode and a bulk-sensitive mode (45° and 90°). The XPS spectra were analyzed to quantify the amount of each component by normalizing their peak area by the sensitivity factor of each core-level orbital.[65] For LSM, *in-situ* XPS experiments were performed in 100 mTorr O_2 at 650°C using the configuration described above at the beamline TEMPO at the synchrotron facility SOLEIL, France.

The surfaces of the films were imaged using high-resolution scanning electron microscopy (HRSEM) and atomic force microscopy (AFM) to reveal the morphology of the surface segregates, which typically precipitate out as particles. HRSEM was measured by a Zeiss Merlin HRSEM with an in-lens secondary electron detector. AFM measurements were performed using a Veeco Metrology Dimension 3100 AFM with a Nanoscope V controller (tapping mode), as well as a Park NX-10 AFM operated in non-contact mode.

The polarization-dependence of Sr surface segregation was measured by means of X-ray photoelectron spectroscopy (XPS), scanning electron microscopy, and atomic force microscopy (AFM). A novel experimental setup provides access to a continuous range of electrochemical potentials on a single sample, ensuring equivalent conditions for each data point. The XPS data acquired on samples heated at 770°C in 1atm O_2 shows a clear enhancement of the segregation of Sr when negative bias is applied to the cathode surface.

2) Effect of surface metal doping

The measurements are performed on $La_{0.8}Sr_{0.2}MnO_3$ thin films grown using pulsed laser deposition using the same deposition recipe as above polarization study. The surface topography was characterized using atomic force microscopy (AFM; Veeco Metrology Dimension 3100 AFM with a Nanoscope V controller; operated in tapping mode). Hf was deposited by physical vapor deposition in ultrahigh vacuum at room temperature using a Focus EFM 3T electron-beam evaporator. The deposition rate was calibrated using a quartz crystal microbalance (Sentys). A thickness of 4Å was selected, approximating a monolayer of deposited material. During deposition one half of the LSM/YSZ samples was covered by Al foil, inhibiting metal deposition on this half of the samples. This geometry allows for a direct comparison of the evolution of untreated and metal-doped LSM by comparing spots at a distance of few millimeters on the same sample in experiments at high temperatures and oxygen pressures.
The APXPS measurements on the effects of metal deposition were performed at beamline 9.3.2 of the Advanced Light Source (Lawrence Berkeley National Laboratory, USA). After transfer the samples were annealed in 1mTorr O_2 at approximately 260°C (as measured by a K-type thermocouple attached to the sample surface) to remove residual C species. The low-temperature reference spectra were taken under these conditions. Spectra of the Sr 3*d*, La 4*d*, Mn 3*p*, O 1*s*, and Hf 4*f* regions were acquired. The photon energies were adjusted to achieve a

kinetic energy of 290eV for all elements in order to achieve comparable mean free paths of the photoelectrons. The Sr 3*d* spectrum was monitored during heating up to the onset of segregation, which was observed at approximately 450°C. The high-temperature effect of metal doping was determined at this onset temperature and at 550°C.

3) Atomic-Scale Surface Structure and Topography

The present project employs a multi-technique approach to investigate the surface properties of $La_{0.8}Sr_{0.2}MnO_3$ (LSM) and their relation to surface stability and degradation. The surface structure and topography has been studied on LSM single crystals, grown using the floating zone method by a collaborating group (Checkelsky Lab, MIT) and cut to expose (001) and (110) facets (cubic notation) by Surface Preparation Laboratory (Netherlands) , as well as epitaxial thin films on commercial $SrTiO_3$ (001) substrates (MTI Corp) grown using pulsed laser deposition (PLD). These samples were mounted on Omicron-type Ta sample plates via spot-welding Ta wire holding the crystal in place. These samples were loaded into ultra-high vacuum (UHV) setups with a base pressure $<2\times10^{-10}$ mbar and equipped with manipulators with heaters based on thermal radiation of a hot filament and high-precision leak valves to set a well-defined background pressure. The scanning tunneling microscopy (STM) images were acquired using a variable-temperature scanning tunneling microscope (VT-STM) (Omicron GmbH, Germany) operated in constant current mode at room temperature; low-energy electron diffraction (LEED) patterns were obtained using SPECTALEED rear-view LEED optics. Prior to the measurements, the samples were heated to 350°C in 2 x 10^{-4}mbar O_2 to remove residual carbon in an UHV preparation chamber, forming part of the setup for STM and LEED.

4) Reversibility of dopant segregation

The measurements are performed on $La_{0.8}Ca_{0.2}MnO_3$, $La0_{.8}Sr_{0.2}MnO_3$, and $La_{0.8}Ba_{0.2}MnO_3$ thin films grown using pulsed laser deposition using the same deposition recipe as above polarization study. Characterization and pre-treatment (dipping into water for 1 min) of samples and were done similarly as described above. Polarizations were applied via lateral polarization or conventional method (single-valued polarization on the whole electrode) at 770°C in 1atm O_2. The amount of surface insulating species was quantified by X-ray photoelectron spectroscopy (XPS) using a Physical Electronics Versaprobe II X-ray photoelectron spectrometer equipped with a monochromated Al Kα X-ray source. *In-situ* electrochemical impedance spectroscopy (EIS) were collected in the frequency range from 1 MHz to 0.1 Hz using an AC voltage amplitude of 10 mV. HRSEM was measured by a Zeiss Merlin HRSEM with an in-lens secondary electron detector. *Ex-situ* X-ray absorption spectroscopy (XAS) measurements were done at the beamline 23-ID-2 at Brookhaven National Laboratory (BNL), USA.

Results and discussion

1) Lateral polarization of $La_{0.8}D_{0.2}MnO_3$ thin film electrodes

Building on the study of cathodic polarization of $La_{0.8}Sr_{0.2}MnO_3$, which was described in the previous progress report, we performed a systematic study of doped $LaMnO_3$ films with three different dopants of the same valence state (Ca, Sr, and Ba) under cathodic and anodic polarization.

1.1. Structure of dense thin-film electrodes:

After deposition and pre-treatment with deionized water, the films were characterized using out-of-plane X-ray diffraction (XRD) and profilometry. As shown in **Figure 1-1**, the XRD patterns of the films show clear peaks corresponding to a (110) orientation (cubic indices), with small components arising also from (100) and (111). The sample thickness is in a range of 80 - 100 nm. In scanning electron microscopy (SEM) images of the as-prepared samples no particles are discernible. XRD spectra acquired after annealing with polarization do not exhibit any significant changes compared to the as-prepared films.

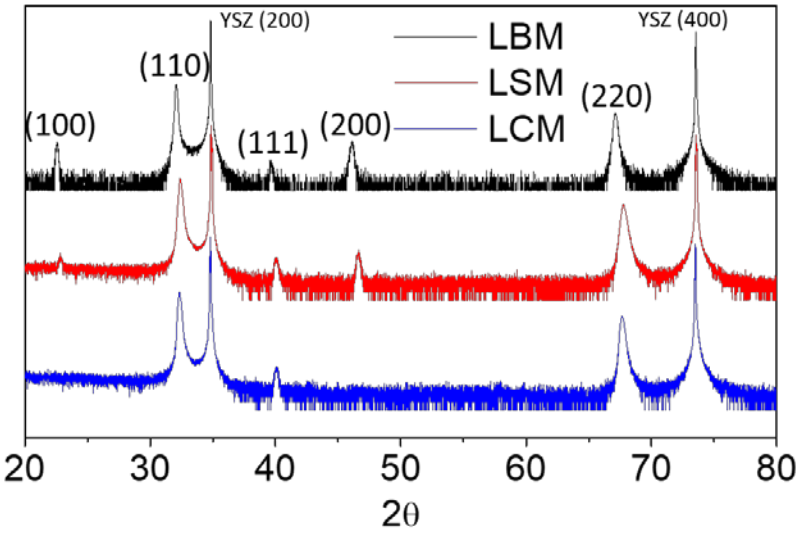

Figure 1-1. XRD patterns of $La_{0.8}Ca_{0.2}MnO_3$ (LCM, blue), $La_{0.8}Sr_{0.2}MnO_3$ (LSM, red), and $La_{0.8}Ba_{0.2}MnO_3$ (LBM, black).

1.2. Potential distribution on the thin film electrode formed by lateral polarization (*in-situ* measurement)

The potential distribution within the LSM film can be illustrated by comparing the peak positions of the La 4*d* spectra at the spots selected for measuring the potential effects. **Figure 1-2** shows the position-dependent La 4*d* peak position as a function of position measured from LSM sample at 650°C in an atmosphere of 100 mTorr O_2.

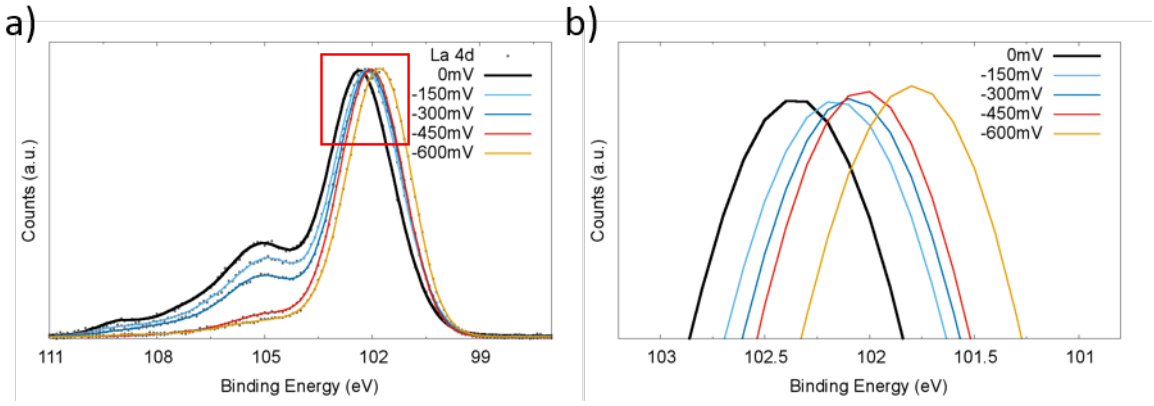

Figure 1-2. La 3*d* spectra acquired at 650°C in five different positions illustrating the gradual change in polarization across the surface: (a) overview (b) zoomed-in view. The position of the La *4d* peak exhibits a continuous monotonic shift with variations of the polarization (nominal values derived from distance) ranging from the working electrode (-600 mV) to the grounded counter electrode. The total shift corresponds to approximately 550 meV.

1.3. Surface chemistry of doped $LaMnO_3$ film electrodes:

X-ray photoelectron spectra of all constituent elements have been acquired to quantify the dopant segregation behavior of LCM, LSM, and LBM. Ca 2*p*, Sr 3*d*, and Ba 4*d* core-levels have been selected for chemical analysis, because they are known to change significantly with bonding environment, and thus, have been widely used in previous segregation studies [19,27,66,67].

Figure 1-3 shows characteristic spectra of the respective dopant species for the as-prepared and annealed films. The spectra have been deconvoluted into two Voigt doublet components: a component at high binding energy, which is commonly attributed to the segregated dopant oxide (green) and a lattice component at low binding energy (blue), corresponding to the original perovskite phase. O 1*s*, La 4*d*, and Mn 3*p* core-level spectra were also acquired to quantify the composition of the surface region. The as-prepared films show low amounts of the respective surface component while the intensity of the lattice component is close to the nominal value of 0.2 in $La_{0.8}D_{0.2}MnO_3$. As a result of annealing, the intensities of the surface components of each dopant increase significantly.

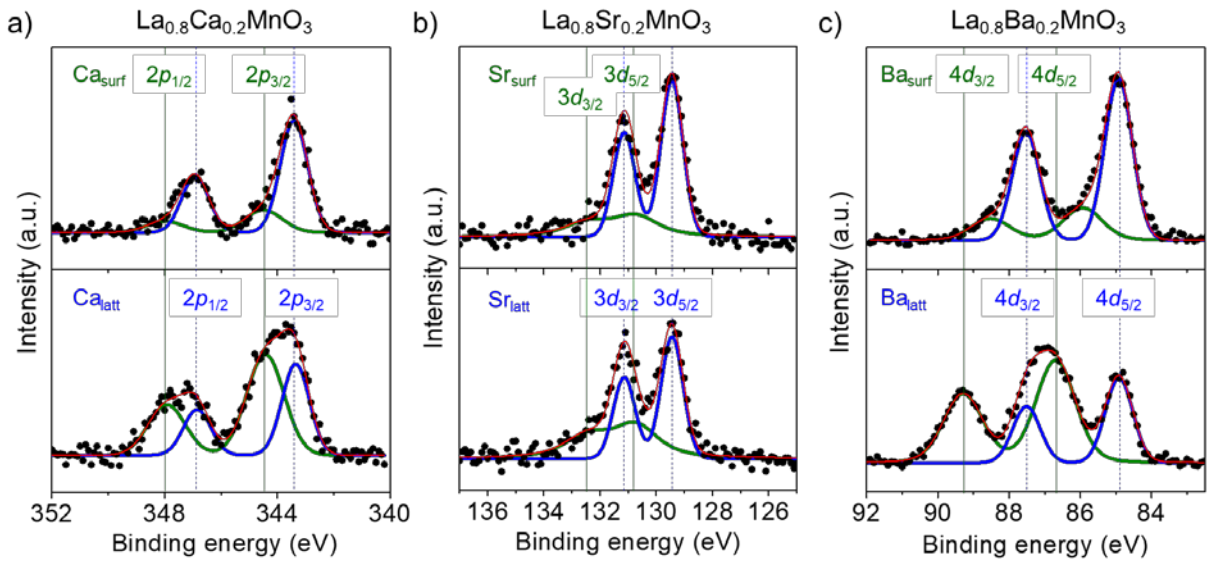

Figure 1-3. Representative core-level X-ray photoelectron spectra of a) Ca 2*p*, b) Sr 3*d*, and c) Ba 4*d*. $La_{0.8}Ca_{0.2}MnO_3$, $La_{0.8}Sr_{0.2}MnO_3$, and $La_{0.8}Ba_{0.2}MnO_3$ films were annealed in pure O_2 for 1 h at 770°C; no bias was applied on the samples shown here. The spectra of the respective as-prepared (top) and annealed (bottom) films were deconvoluted to show lattice (blue) and surface (green) species.

In virtue of the lateral polarization method, only two films were required to take 9 different sets of spectra (or even more if needed), eliminating potential errors resulting from different sample preparation and history. **Figure 1-4** describes the progressive changes in each dopant core-level spectrum (Ca 2*p*, Sr 3*d*, and Ba 4*d*) with the gradual shift from positive to negative potential. Given the positions at the surface, at which these spectra were taken, the corresponding potentials are assigned as ±160 mV, ±320 mV, ±480 mV, ±640 mV, -750 mV, based on the approximately linear relation of position and potential observed in synchrotron photoemission measurements (**Figure 1-2**). The intensity of each spectrum was normalized by the amount of total A-site cations. By deconvoluting each spectrum as illustrated in **Figure 1-4**, the respective segregated component, Ca_{surf}, Sr_{surf}, and Ba_{surf}, can be quantified as a function of the electrochemical potential. The amounts of segregation in the different oxides can also be visually recognized when tracking the relative intensities of the points highlighted by the dashed lines at two different binding energies: 344.5 and 343.5 eV for LCM, 130.8 and 129.1 eV for LSM, and 89.3 and 85 eV for LBM. In case of LCM, it is observable from **Figure 1-4a** that both the absolute and relative intensity of the surface component (Ca_{surf} $2p_{3/2}$, 344.5 eV) continuously increase compared to the lattice component (Ca_{latt} $2p_{3/2}$, 343.5 eV) as potential decreases. For the case of LBM shown in **Figure 1-4c**, both the absolute and relative intensity of the surface component (Ba $4d_{3/2}$, 89.3 eV) decrease with a potential drop to -480 mV but increase again as potential becomes more negative. While for LCM and LBM the higher binding energy peak corresponds well to the location of a sub-peak of the surface component, the energy of 130.8 eV has been selected for the case of LSM, since it is best suited for following changes in the Sr 3*d* peak shape. The peak at

130.8 eV contains intensity contributions of both surface and lattice component. Thus, comparing it with the peak at 129.1 eV (purely Sr_{latt} $3d_{5/2}$) provides a rough estimate of the amount of segregation. Also, the increase in the high-binding energy shoulder between 131 and 133 eV is an indicator of segregation. It can be seen in **Figure 1-4b** that the segregation becomes less as potential goes down to 160 mV but increases again when moving to more negative potentials.

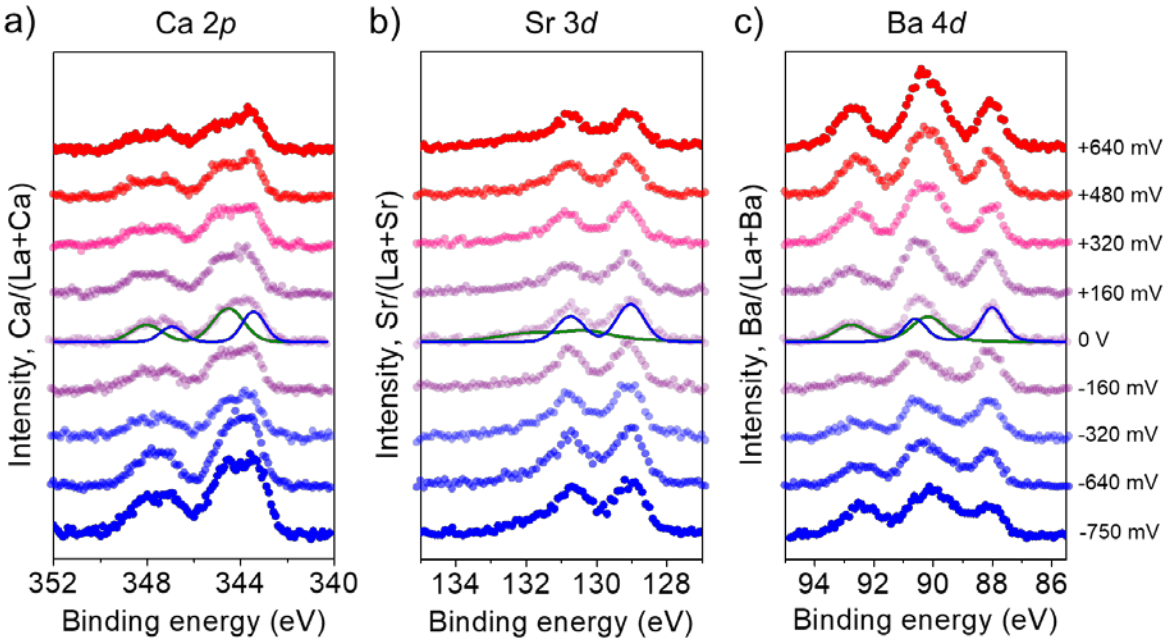

Figure 1-4. X-ray photoelectron spectra taken for Ca 2*p*, Sr 3*d*, and Ba 4*d* illustrating the extent of dopant segregation at the surface as a function of applied potential at 770°C in 1 atm O_2 for 1 h for a) $La_{0.8}Ca_{0.2}MnO_3$, b) $La_{0.8}Sr_{0.2}MnO_3$, and c) $La_{0.8}Ba_{0.2}MnO_3$. The 0 mV spectrum in each core-level is deconvoluted into the emission arising from the surface (green) and lattice (blue) binding environments.

Figure 1-5 shows the intensity of the respective surface components normalized by the total peak area of the A-site cations, plotted as a function of the applied potential. In all three compounds, the surface contribution of the dopant is found to increase towards higher negative polarization values within a particular potential range: -754 to 640 mV for LCM (**Figure 1-5a**), -754 to 160 mV for LSM (**Figure 1-5b**), and -754 to -480 mV for LBM (**Figure 1-5c**). The ranges vary substantially between the three compounds, illustrated by the clear shift of the point of minimum segregation. In the cases of LSM and LBM, for which the dopant has a larger cation radius than La, segregation increases also with increasing anodic polarization, leading to a minimum in the potential-dependent intensity of the surface component. A monotonic increase in segregation is observed from 160 mV to 640 mV for LSM and -480 mV to 640 mV for LBM. For all three compounds, the segregation curve exhibits a sharp transition point, a minimum in the cases of LSM (160 mV) and LBM (-480 mV) and the change between steep and flat potential-dependence of segregation for

LCM (-480 mV). The corresponding potential of minimum segregation shifts towards more negative values with increasing dopant radius.

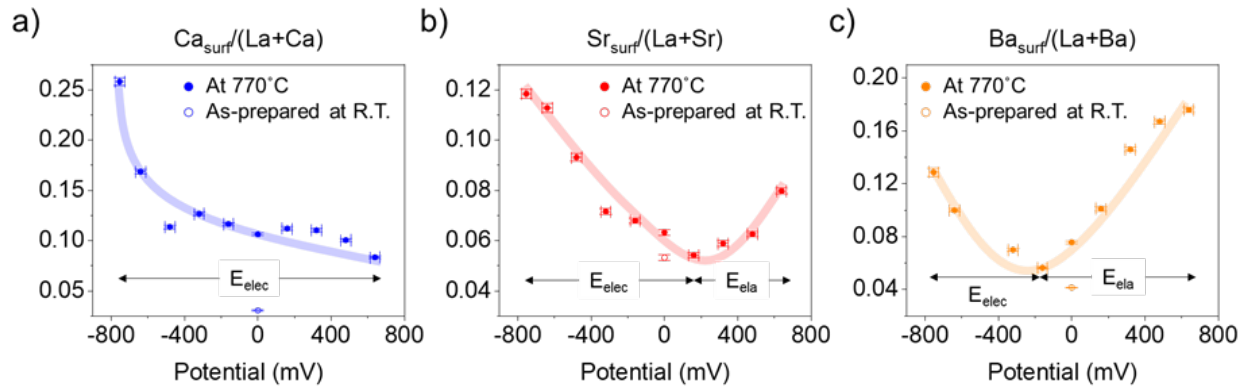

Figure 1-5. XPS intensity of surface a) Ca, b) Sr, and c) Ba components, normalized by the total intensity of A-site cations of $La_{0.8}Ca_{0.2}MnO_3$, $La_{0.8}Sr_{0.2}MnO_3$, and $La_{0.8}Ba_{0.2}MnO_3$, respectively. The filled circles indicate the data points from the polarized samples annealed at 770°C in 1 atm O_2 for 1 h. The open circles indicate the data points from the as-prepared samples. The arrows in the graphs indicate the regions where the electrostatic energy or elastic energy is the dominant reason of segregation of the dopant. The thick trend lines serve only as a guide to the eye.

1.4. Surface morphology of doped $LaMnO_3$ thin-film electrodes:

The differences in surface topography due to dopant segregation have been analyzed by SEM and AFM, as shown in **Figures 1-6** and **1-7**. For LSM and LBM, the surface at the highest negative (cathodic) potential (-750 mV) is populated by small particles (**Figure 1-6b**, left and **1-6c**, left). However, the species on LCM exhibit a granular structure consisting of particles of similar size, covering its entire surface (**Figure 1-6a**, left). Under the most positive (anodic) potential (+640 mV), the surfaces of LSM and LBM are characterized by the formation of smaller particles than those under the negative potential, whereas LCM does not exhibit any discernible features. Further SEM images of LSM and LBM were acquired under the potentials showing the lowest segregation in XPS, +160 mV and -160 mV, respectively. For LCM, +160 mV was selected as an intermediate step.

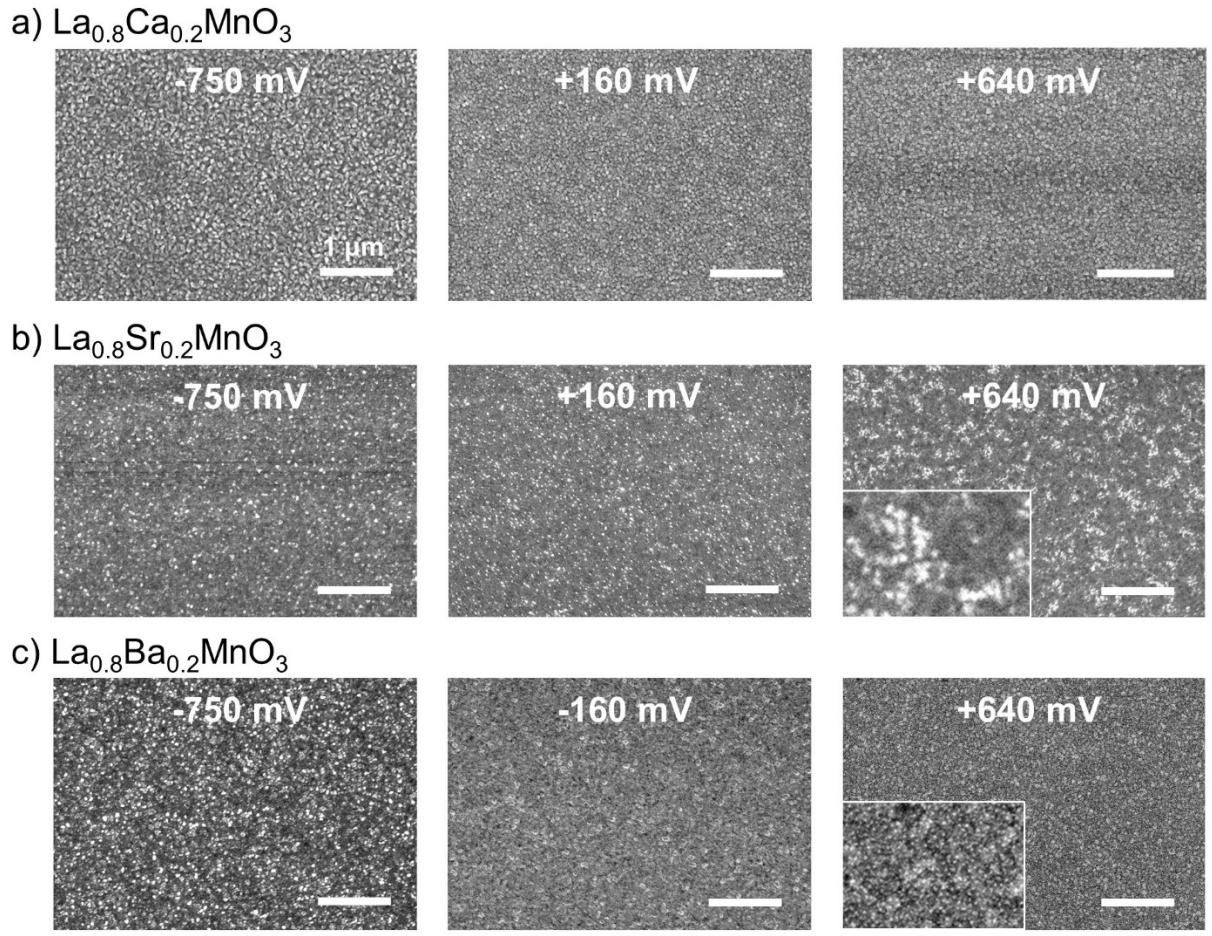

Figure 1-6. SEM images of the $La_{0.8}Ca_{0.2}MnO_3$, $La_{0.8}Sr_{0.2}MnO_3$, and $La_{0.8}Ba_{0.2}MnO_3$ surfaces after annealing at 770°C in 1 atm O_2 under polarization, acquired at different locations corresponding to the indicated bias voltages. a) $La_{0.8}Ca_{0.2}MnO_3$ at -750 mV, +160 mV, and +640 mV, b) $La_{0.8}Sr_{0.2}MnO_3$ at -750 mV, +160 mV, and +640 mV, and c) $La_{0.8}Ba_{0.2}MnO_3$ at -750 mV, -160 mV, and +640 mV. The magnification of all the images is 25k with a scale bar indicating 1 µm. Insets in $La_{0.8}Sr_{0.2}MnO_3$ and $La_{0.8}Ba_{0.2}MnO_3$ at +640 mV are 4-times further magnified images for a clearer view of small particles on their surface.

The influence of the applied potential on the surface roughness has been also been assessed using AFM. **Figure 1-7** summarizes the AFM results and provides a comparison of the three compounds. Images (a-c) illustrate the surface topography after annealing at high negative (-670 mV) and positive (+670 mV) potentials in pure O_2 for 1 h at 770°C. Tiny particles observed by SEM on the most positive side of LBM (the inset in **Figure 1-6c**, right) were not observed by AFM. Graphs at the bottom of **Figure 1-7** show the trend in roughness values from the matrix phase (particle free zones) of each film surface. The root-mean-square (RMS) roughness (blue line) shows a clear common trend towards smoother surfaces at positive potentials for LCM and LBM. Especially for LCM, the evolution of surface roughness matches well with the evolution of Ca_{surf}

as quantified by XPS in **Figure 1-7**. However, LSM does not exhibit any clear trend in the roughness and very little overall variation. The large error bar for LCM at -670 mV results from a coexistence of rough and flat patches at the surface.

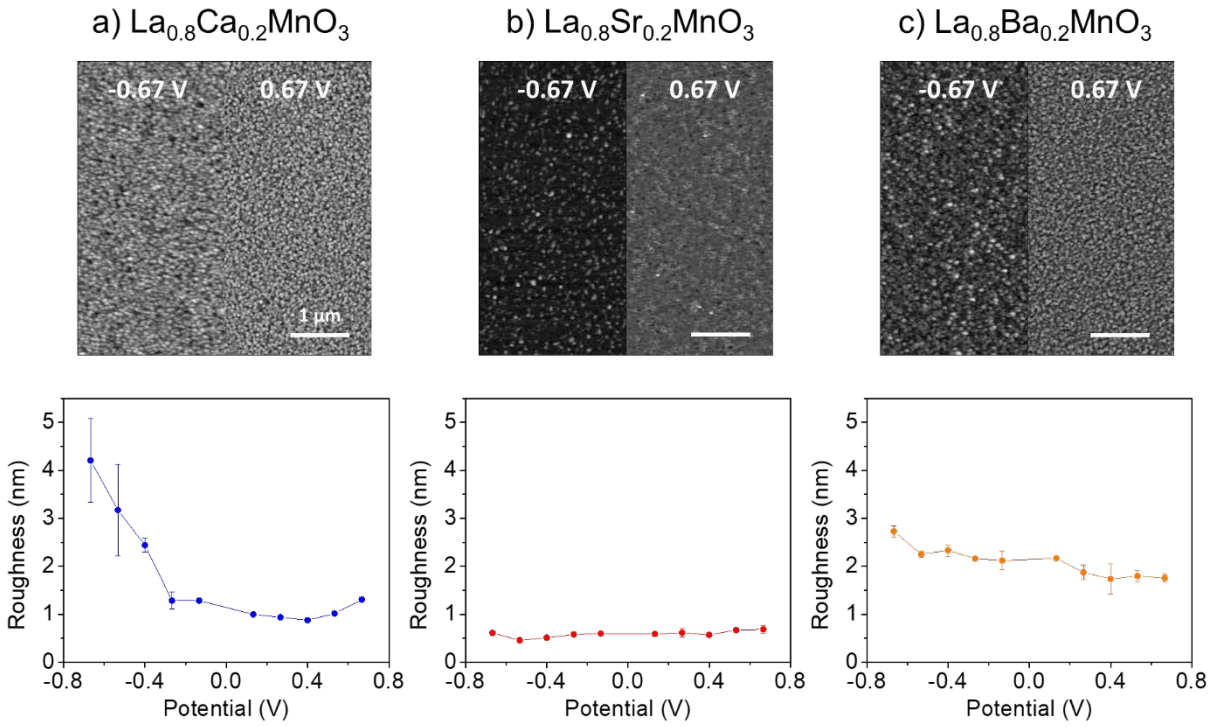

Figure 1-7. AFM images (top) and AFM roughness (bottom) measured for (a) $La_{0.8}Ca_{0.2}MnO_3$, (b) $La_{0.8}Sr_{0.2}MnO_3$, and (c) $La_{0.8}Ba_{0.2}MnO_3$. AFM images were taken at -0.67 V (left) and + 0.67 V (right). AFM roughness was measured by the variation of the root-mean-square (RMS) roughness of the surface layer (excluding particles) and the particle volume per µm² and is plotted as a function of bias voltage.

1.5. Further discussion

The present results on surface degradation in a lateral polarization gradient demonstrate both, differences and similarities of the three compounds under scrutiny: In LCM, LSM, and LBM dopant cations segregate to the surface at high temperature (770°C) and form chemically different surface species. In highly reducing conditions the extent of segregation increases [37] for all three compounds, whereas under oxidizing conditions an enhancement is only observed for LSM and LBM. The XPS results display dopant-specific trends of the extent of segregation as a function of bias voltage showing; a sharp transition between two regimes of segregation behavior is observed for each compound. These trends also find representation in gradual changes observed in SEM and AFM images.

Here, we relate the polarization-dependent segregation behavior of the three different compounds to varying contributions of the two driving forces of segregation outlined in the

introduction: an elastic and an electrostatic force. Their balance in causing the segregation of the different dopants at different oxygen chemical potentials is subject of the two main hypotheses tested in the present report: 1) E_{elec} increases with a decrease in effective pO_2 and 2) E_{ela} increases with an increase in effective pO_2 for all three compounds in the present study. The first hypothesis is related to the trend for increasingly negative potentials. For all three compounds, segregation is indeed increasing at high negative potentials, corresponding to reducing conditions: -754 to 640 mV for LCM, -754 to 160 mV for LSM, and -754 to -480 mV for LBM. Entering the regime of high oxygen vacancy concentrations thus leads to enhanced segregation. The *in-situ* data for cathodically polarized LSM in **Figures 1-2** support these results; the high surface sensitivity even substantially enhances the differences observed between the points. Under reducing conditions, the reported chemical expansion of perovskite oxides [68] diminishes the importance of the elastic energy. The electrostatic energy, on the other hand, increases with the expected rise of the oxygen vacancy concentration upon reduction of the surface. Thus, the observed increase at decreasing effective oxygen pressures is in good agreement with hypothesis 1. However, as the potential becomes more positive and the conditions more oxidizing, the lattice parameter of $LaMnO_3$ decreases [21,69], raising the elastic energy contribution for larger dopants substituting La, in this case Sr and Ba. At the same time, the number of oxygen vacancies at the surface decreases and so does the electrostatic energy. These simultaneous changes occurring in the oxide films cause the nature of the dominant driving force to transition from electrostatic to elastic. Since Ca is the smallest of the three dopants and exhibits barely any size mismatch with La, the contribution from the elastic energy is negligible for Ca. Hence only the effect of a decrease in electrostatic energy is observed to modify the extent of segregation, manifesting itself as a continuous decrease throughout the graph in **Figure 1-5a**. The existence of a transition point to a flatter potential-dependence, however, indicates that there is a discernible contribution of E_{ela} even under mildly reducing conditions, but under neither of the conditions investigated it is sufficient to overcome the overall decrease caused by the drop in E_{elec}. With increasing cathodic polarization, E_{elec} begins to fully dominate the observed behavior as soon as the potential is sufficiently negative to induce substantial reduction. For LSM, a clearer transition is observed. However, the effective pO_2 at the transition between the two regimes is substantially higher than in the case of LCM. The larger cation mismatch between Sr and La significantly increases the importance of E_{ela} compared to Ca. Under increasingly oxidizing conditions, segregation of Sr is progressively enhanced. This behavior is found to be even more prominent in LBM owing to its larger cation radius. The intrinsically high misfit elastic energy of Ba in LBM grows further as pO_2 increases. The large dopant size results in a predominantly elastically driven segregation behavior already at the reducing condition of -480 mV. These results coincide well with our initial expectations for dopants with different cation radii. The observations indicate that the second hypothesis is based on a correct concept even though the rise in elastic energy is not sufficient for Ca to enter an elastically dominated regime. The clear increase in segregation at high cathodic polarization for all three compounds strongly supports the first hypothesis of a common electrostatic driving force.

In agreement with the spectroscopy results, measurements of the surface topography using SEM (**Figure 1-6**) and the particle volume and roughness using AFM (**Figure 1-7**) display a gradual change across the surface of LCM and LBM. The low level of segregation and the variations in particle shape and surface topography of LSM may conceal a comparable trend. In the case of LBM, a comparison of the particle volume and the contribution of the segregated species to the Ba 4*d* spectra shows very good agreement. This close correspondence allows us to assign the preferential growth mode of BaO_x as Volmer-Weber type (3D particles). The clear difference in particle shape indicates the possibility of different surface phases under reducing and oxidizing conditions. For LCM segregation clearly proceeds in a different manner: No distinct particles protruding from the surface layer are observed at any condition, but the overall surface roughness is found to grow dramatically for increasingly negative potentials. This can be interpreted as the growth of a rough two-dimensional oxide layer of precipitates wetting the LCM surface. The change in surface roughness could be attributed to the growth of a flat but granular structure rather than the presence of a smooth 2D wetting layer. These two cases, however, are expected to be indistinguishable in XPS experiments.

2) Effect of surface metal doping

2.1. The effect of Hf on Sr segregation

In synchrotron-based ambient-pressure XPS experiments we investigated the effect of metal doping of the surface on the stability of $La_{0.8}Sr_{0.2}MnO_3$ thin-film model cathodes on a YSZ electrolyte single crystal. We directly compare an untreated half of one single LSM sample with the second half modified by electron-beam deposition of 4Å of Hf or Ti. **Figure 2-1** provides a comparison of Sr 3*d* spectra of the unmodified side of LSM at low temperature and at 450°C acquired *in situ* in 1mTorr O_2. The deconvolution of the peaks shows two species: Sr in the LSM lattice (Sr_{latt}) and a surface phase of Sr (Sr_{surf}), assigned as the segregating SrO_x species. While Sr_{latt} dominates the spectrum at low temperature, the Sr_{surf} contribution increases substantially when heating to 450°C.

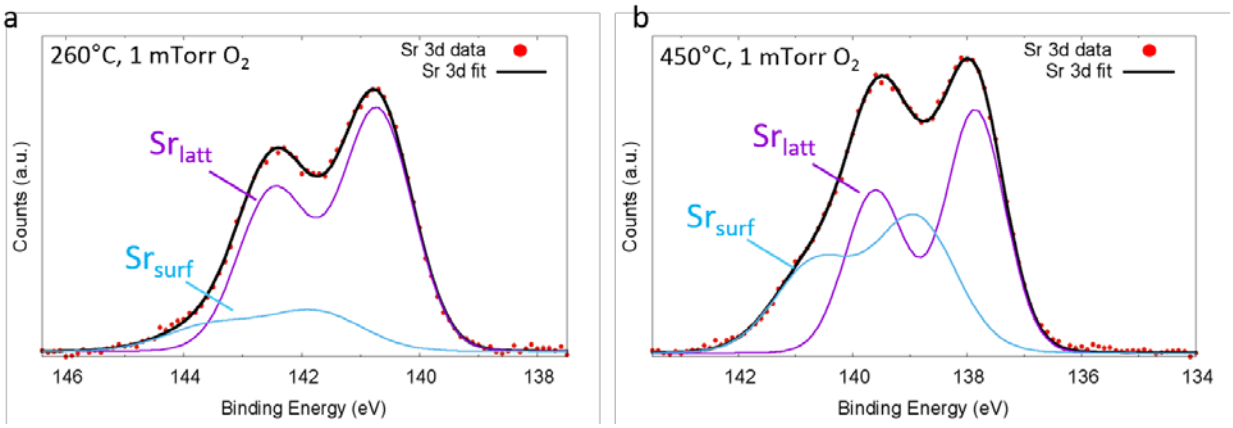

Figure 2-1. Sr 3*d* spectra of $La_{0.8}Sr_{0.2}MnO_3$/YSZ acquired in-situ in 1mTorr O2 at 260°C (a) and 450°C (b). The deconvolution shows two species, Sr in the $La_{0.8}Sr_{0.2}MnO_3$ lattice (Sr_{latt}, purple) and the segregating SrO_x species (Sr_{surf}, cyan). At 450°C a substantial increase in Sr_{surf} is observed, corresponding to surface segregation of Sr.

On the side modified by Hf a similar effect was observed, but the increase in Sr_{surf} was found to be substantially lower. **Figure 2-2** shows a comparison of the cation intensity ratios measured on the Hf-doped and the unmodified halves of the sample at room temperature and during annealing at 450°C (two spots of each side) and at 550°C. While different descriptors display small differences in the trends, all graphs clearly show a higher intensity in surface Sr and total Sr in the case without Hf. In **Figure 2-2a**, the ratio of Sr_{surf} to Sr_{latt} shows an overall enhancement of the surface Sr species on the undoped side of the sample, but at higher temperature the overall Sr content increases substantially, leading even to a decrease in **Figure 2-2a**. The increase in total Sr content is, however, very clear for the Sr/Metals ratio shown in **Figure 2-2d**. The overall intensity of Sr_{surf}, on the other hand, increases monotonically with temperature, illustrated by the Sr_{surf}/(Sr+La) and the Sr_{surf}/Metals ratios on display in **Figure 2-2b** and **2-2c**.

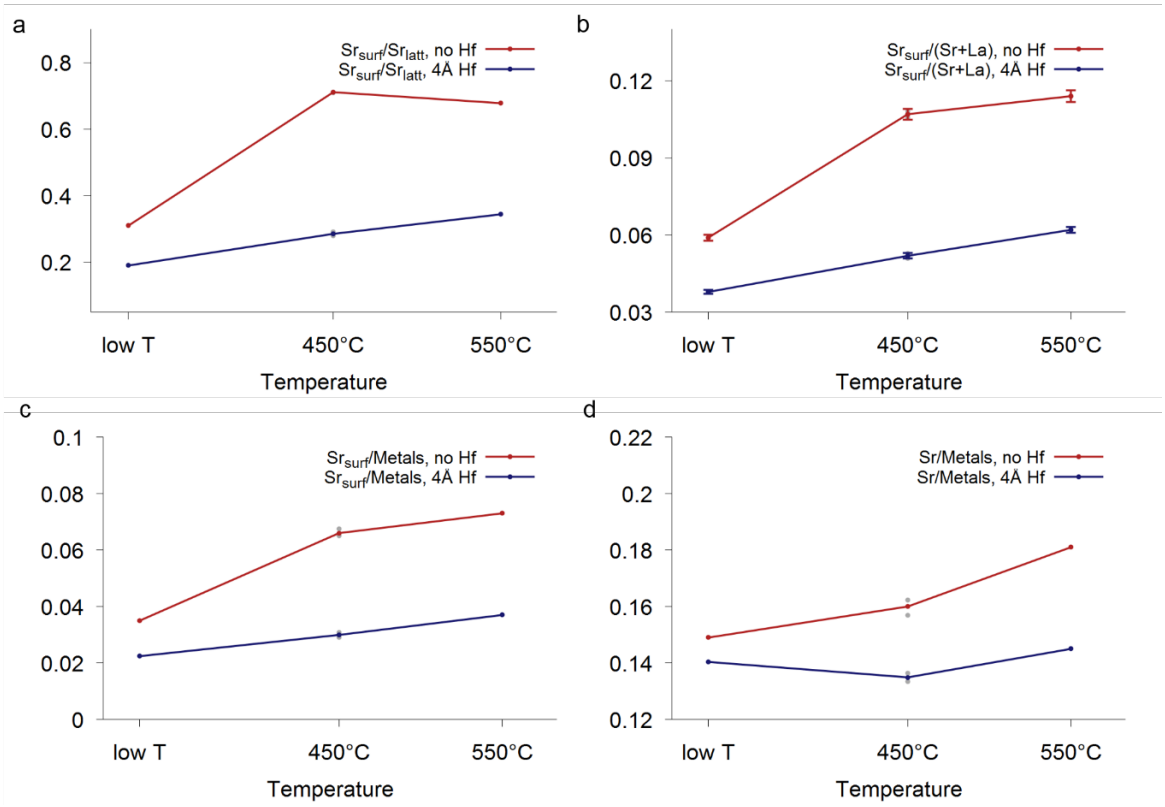

Figure 2-2. Quantification of Sr segregation on $La_{0.8}Sr_{0.2}MnO_3$/YSZ with/without prior deposition of Hf. Intensity ratios at room temperature, 450°C (two points), and 550°C on an area with 4Å Hf (blue) and without Hf (red): (a) Ratio of segregated surface Sr (Sr_{surf}) to Sr in the $La_{0.8}Sr_{0.2}MnO_3$ lattice (Sr_{latt}). (b) Ratio of Sr_{surf} to the total A-site cation intensity (Sr+La). (c) Ratio of Sr_{surf} to the sum of all cations. (d) Ratio of total Sr to the total cation intensity. In all cases the relative intensity of Sr_{surf} and total Sr content is higher without Hf doping and increases more strongly with heating.

Figure 2-3 illustrates the direct relation of Sr_{surf} content and Hf coverage in a line scan across the surface, moving on a linear path from the Hf-modified region to the undoped half of the sample in 8 steps. In **Figure 2-3a** four representative Sr 3*d* spectra are presented, which were acquired along the path: (1) Hf-containing side, (3) transition zone with low Hf content, and (5, 7) undoped side. **Figure 2-3b** displays the Sr_{surf}/Sr_{latt} ratio in direct comparison to the Hf content in the 8 spots included in the line scan. The increase in Sr_{surf} clearly follows the decrease in Hf intensity throughout the entire line scan. The figure illustrates the direct relation of Sr_{surf} content and Hf coverage in a line scan across the surface, moving on a linear path from the Hf-modified region to the undoped half of the sample in 8 steps.

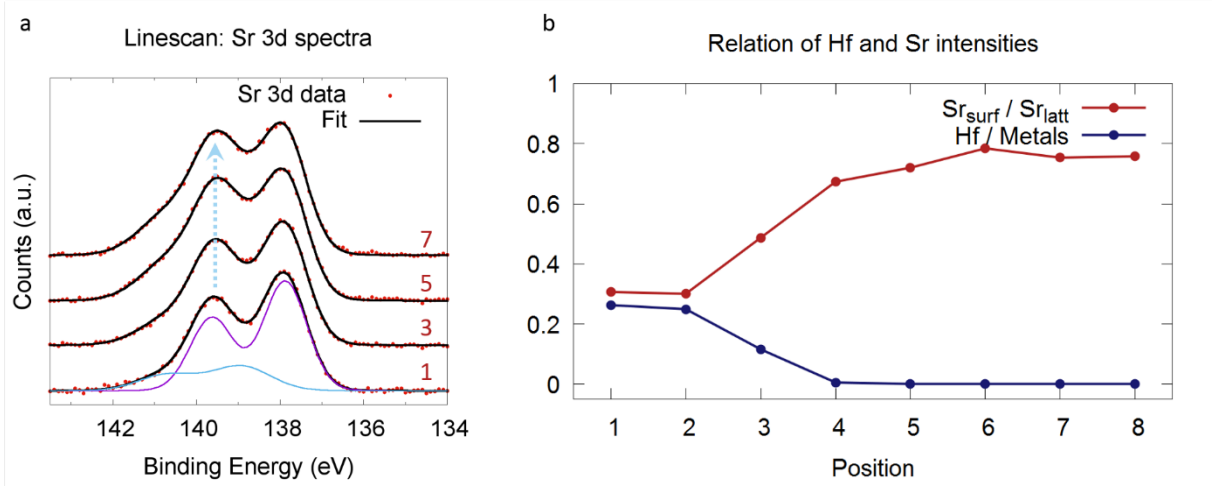

Figure 2-3. Line scan across the $La_{0.8}Sr_{0.2}MnO_3$ thin film at 450°C in 1.3×10^{-3} mbar O_2. (a) Sr 3d spectra in four positions in different locations moving from the Hf-doped side (1) via a transition zone with low Hf content (3) to the undoped region (5, 7). Segregation increases with decreasing Hf content. (b) Relation of Hf content and Sr_{surf}/Sr_{latt} ratio in 8 points along a linear path across the sample. Sr_{surf}/Sr_{latt} shows a direct, inverse dependence on the Hf content.

In addition to the spectroscopy experiments, the surface was imaged using atomic force microscopy and scanning tunneling microscopy (insets of **Figure 2-4**). **Figure 2-4** shows a comparison of AFM and STM images acquired *ex-situ* after the XPS experiments described above. A grainy structure with a root-mean-square roughness of ≈0.96-0.98nm is observed in large-scale AFM images ($4.5\times4.5\mu m^2$, Δz=6.5nm) in points without Hf (**Figure 2-4a**) and with deposition of 4Å of Hf (**Figure 2-4b**) after the annealing experiments. The STM images in the insets ($200\times200nm^2$, Δz=7.5nm) do not reveal any discernible differences in the shape and size of the observable features. The high, bright feature in the center of **Figure 2-4a** is considered a dust particle or contaminant, since similar particles are observed in random distribution in all positions on the sample.

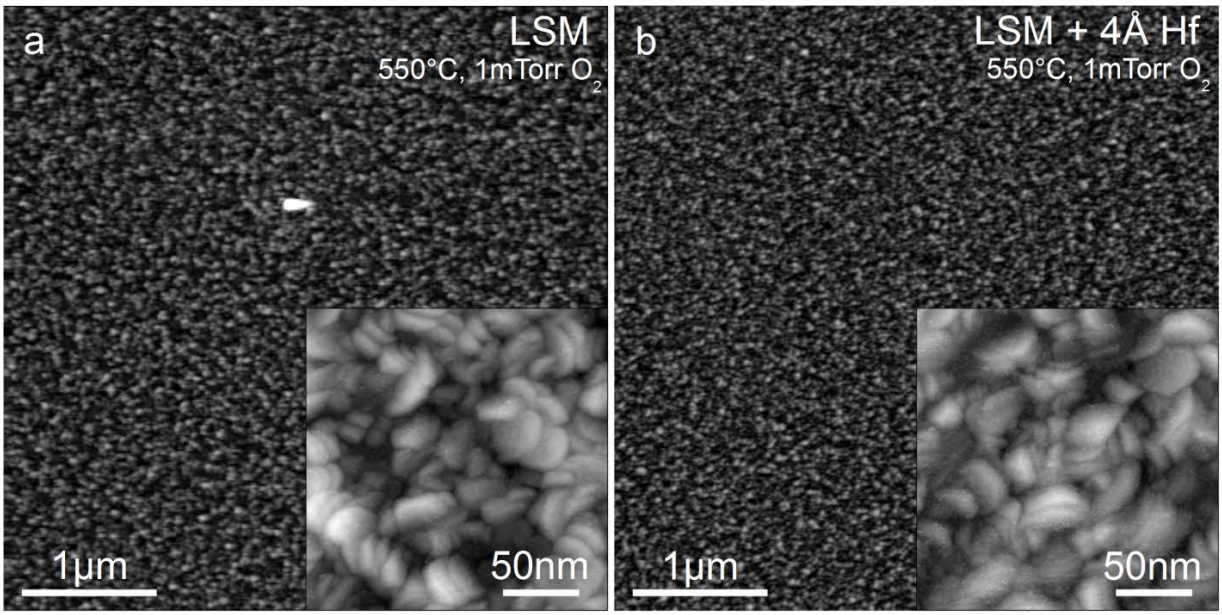

Figure 2-4. Atomic force microscopy and scanning tunneling microscopy (insets) images of $La_{0.8}Sr_{0.2}MnO_3$ acquired after the *in-situ* XPS measurements at up to 550°C in 1mTorr O_2 in regions without (a) and with (b) prior Hf deposition. Both the root-mean-square roughness (≈0.96-0.98 nm in the AFM images) and the average feature shape and size are very similar. The bright feature in the center of (a) is considered unrelated to Sr segregation; a random distribution of comparable particles is observed on the entire sample.

2.2. Further discussion

Our results clearly demonstrate the stabilizing role of modifying the surface of the high-temperature SOFC cathode material LSM with low coverage of Hf deposited by electron-beam evaporation. These results are not only in good agreement with previously reported stability-enhancement of $(La,Sr)CoO_3$, but also demonstrate that this impact of metal deposition is not specific to one material or deposition method. Specifically, the present work utilizes electron-beam evaporation, which does not induce any secondary changes to the surface, and the high-temperature cathode material $(La,Sr)MnO_3$, exhibiting intrinsically different properties and operation mechanisms from the low-temperature oxygen conductor $(La,Sr)CoO_3$.

Here, an *in-situ* analysis of the stabilizing effect of vapor-deposited Hf on LSM surfaces is presented. Hf, a 5*d* transition metal that interacts strongly with oxygen, has been selected for this study due to it extremely low reducibility and since its strong stabilizing effect on the surface of LSC [50]. Both temperature- and coverage-dependent XPS data show that Hf also has a clear effect reducing the extent of Sr segregation in LSM. While a general enrichment in the segregated component Sr_{surf} is observed also in the presence of Hf, the modification of the surface with Hf clearly diminishes its intensity as well as the overall Sr enrichment of the surface region accessible to XPS. This becomes apparent when increasing the temperature to 550°C, resulting in a strong increase in the total Sr content (**Figure 2-2d**), contrasted by a decrease in the Sr_{surf}/Sr_{latt} ratio

compared to the value at 450°C (**Figure 2-2a**). Clearly, this also affects the descriptors Sr_{surf}/(Sr+La) and Sr_{surf}/Metals (**Figures 2-2b** and **2-2c**) and leads to an under-representation of the Sr_{surf} content. The role of Hf is most strongly conveyed by the position-dependent analysis presented in **Figure 2-3**, which shows an unambiguous correlation between lower Sr_{surf} content and the presence of Hf. The intermediate level of segregation in the transition zone between Hf-doped and unmodified side provides evidence that the stability enhancement scales with the deposited coverage in the sub-monolayer regime. The stabilizing effect observed for Hf vapor-deposited at room temperature also highlights the importance of the surface composition in Sr segregation. Were bulk effects to dominate the segregation behavior, the highly localized Hf-containing layer would only have a negligible effect on the distribution and precipitation of Sr-based species. We therefore attribute this stabilizing effect of Hf deposition to a decrease in surface reducibility of LSM, which results in a lower oxygen vacancy concentration and thus in a lower electrostatic driving force of segregation, comparable to results reported for $La_{0.8}Sr_{0.2}CoO_3$ [50]. This interpretation is based on the fact that no changes in the chemical state or the intensity ratios of other elements in LSM were observed in the presence of Hf. Such changes would be expected for example for the formation of an entirely different surface phase involving Hf. Moreover, **Figure 2-3** indicates that up to the investigated coverage of 4Å the strength of the observed effect scales with the amount of Hf that is deposited, comparable to doping rather than a closed layer of a different phase.

3) Atomic-Scale Surface Structure and Topography

3.1. Scanning tunneling microscopy (STM) measurement on LSM thin films

The (110) and (001) surfaces (cubic notation) of LSM have been studied using scanning tunneling microscopy and low-energy electron diffraction of LSM single crystals and thin films on $SrTiO_3$. To our knowledge, our measurements are the first reports of STM measurements on LSM single crystals. For all samples a high surface roughness was observed, borne out by a high step density in STM images and broad, weak diffraction spots in LEED patterns. For thin-film samples, this could partially be improved by reducing the thickness of the films, requiring to use Nb-doped $SrTiO_3$ substrates for conductivity.

Figure 3-1 show large-scale STM images of an as-grown LSM/STO (001) surface after annealing in 2×10^{-4}mbar O_2. The surface is even, but the LSM layers are not closed. The terraces exhibit a high density of islands and holes with an approximate step height of 3.5-4Å, in agreement with a single unit cell of LSM. Examples of this type of steps are indicated by the blue arrows. The orange rectangle in **Figure 3-1a** marks the region, where the image in **Figure 3-1b** was acquired. In the magnified view, a high density of particles the surface is discernible (examples highlighted by red arrows). Since Sr segregation occurs already during the growth of LSM thin films and no

contaminants or C-related species could be observed in XPS, these particles are assigned as SrO_x precipitates.

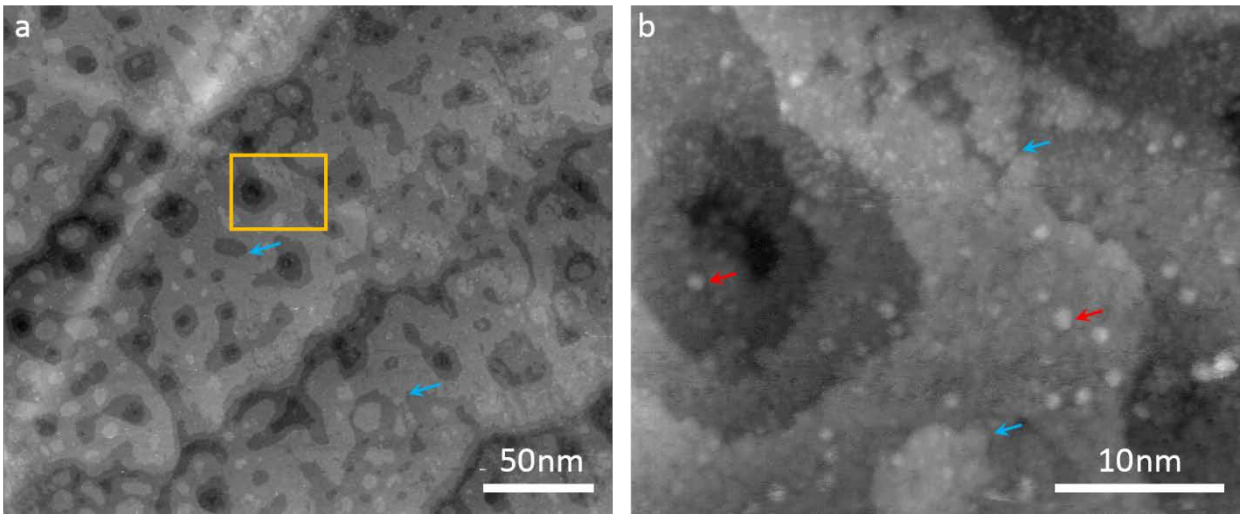

Figure 3-1. STM images of $La_{0.8}Sr_{0.2}MnO_3/SrTiO_3(001)$. a) Overview image showing LSM terraces with pits and islands characterized by steps of a height of ≈3.5-4 Å. The orange box indicates the location, where the detailed image in (b) was acquired. The blue arrows indicate examples of step sites. The red arrows in (b) indicate SrOx particles that are present after growth.

This interpretation is supported by the observations presented in **Figure 3-2**, which was acquired after cleaning the as-grown sample in deionized water, which is expected to dissolve the SrO_x species. Indeed, the particles are no longer present. The surface, however, undergoes further roughening; additional holes in the terraces are observed. For this preparation it was possible to acquire high-resolution images, such as the one presented in **Figure 3-2a**. The inset highlights an area, in which a square arrangement of atomic-scale features could be resolved. The black, blue, and red lines in the inset indicate the locations, which were selected for the line scans presented in **Figure 3-2b**. The measured distances (≈3.5Å) are comparable to a primitive LSM unit cell. A square periodicity can also be derived from LEED patterns, such as the one presented in **Figure 3-2c** (electron beam energy: 65eV). The cyan square indicates the primitive unit cell of a bulk-terminated LSM structure with its length corresponding to the unit cell size of LSM. Additional spots (highlighted by the yellow square) indicate the existence of a surface reconstruction.

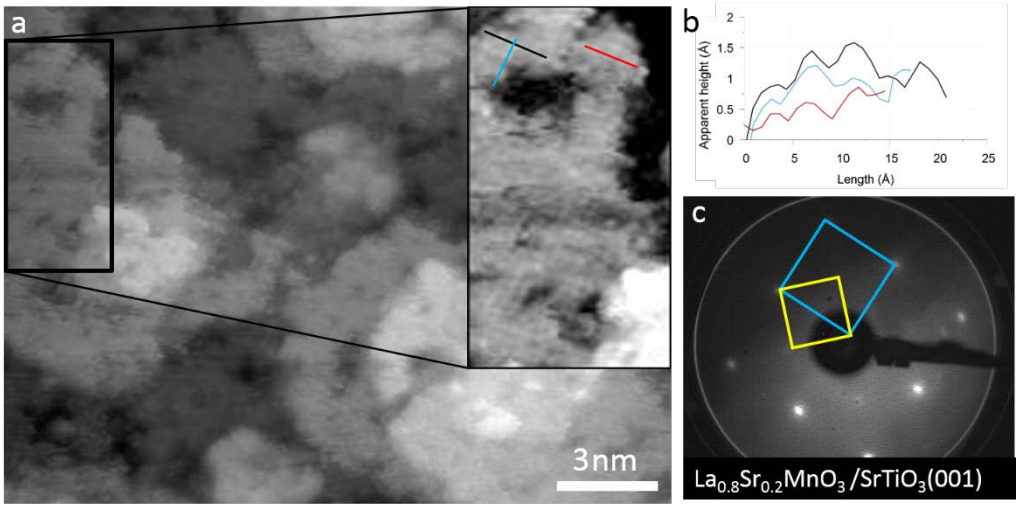

Figure 3-2. STM and LEED of $La_{0.8}Sr_{0.2}MnO_3/SrTiO_3(001)$ after *ex-situ* H_2O treatment. a) Close-up image showing LSM terraces of single-layer height. No SrOx particles are discernible, but dark spots are observed on the terraces. In the magnified image a square arrangement of atoms at the surface can be seen. The corrugation is illustrated by the line scans plotted in (b). c) LEED pattern (E_{e^-}=65eV) of the surface preparation corresponding to the image in (a). A square pattern of approximately the size of a primitive LSM unit cell is observed, which is in agreement with the structure in the STM image in (a). The yellow square highlights weak spots indicating a surface reconstruction.

3.2. Scanning tunneling microscopy (STM) measurement on LSM single crystals

While in these films on $SrTiO_3$ the film properties are influenced by the substrate, LSM single crystals reflect the pure material's properties. One of the aims of the surface science study of LSM is finding a reproducible preparation of high-quality LSM surfaces. **Figure 3-3** shows an STM image acquired after sputtering of an LSM (001) crystal and annealing at 700°C in 5×10^{-6} mbar of oxygen. The surface is rough, with series of single-unit-cell steps and small flat areas (diameter < 10nm). The LEED pattern in the inset exhibits a square arrangement of diffraction spots, which are, however, weak and broad. This is in agreement with an ordered structure, which is present across the entire surface, but limited to small patches straddling the limits of the coherence length of LEED.

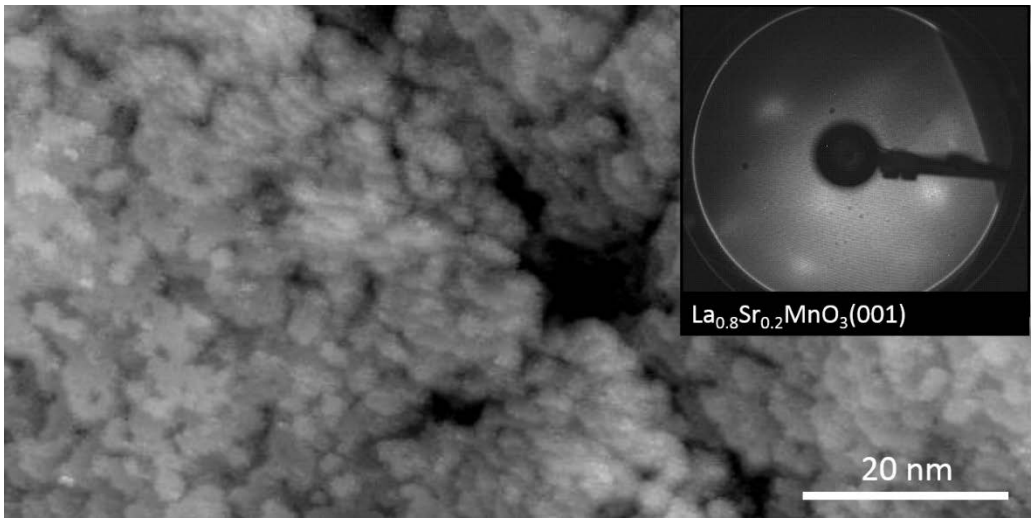

Figure 3-3. STM and LEED of $La_{0.8}Sr_{0.2}MnO_3(001)$, sputtered and annealed at 700°C. The surface is rough with a maximum continuous size of terrace below 10nm. LEED (E_e = 32 eV) shows an ordered square structure, but the small terrace sizes lead to weak, broad diffraction spots.

Figure 3-4 demonstrates the effects of annealing an LSM (001) crystal in 2×10^{-5}mbar at 600°C in an UHV chamber. Even without prior sputtering, carbon-based species can be removed and a surface based on clean LSM terraces is exposed, as shown in **Figure 3-4a**. The zoomed-in view in **Figure 3-4b** illustrates small, flat terraces with holes and small particles, but it also demonstrates the coexistence of small areas of a different surface termination. The small areas highlighted by the cyan arrows present a row-like structure with row distances of 0.8-1 nm, but are flat on the given size scale. The step height between the two terminations amounts to approximately 2Å in all cases. The atomic-scale image in **Figure 3-4c** also shows a row-like structure on the predominant, flatter surface termination. Here, the row distance is in agreement with 3.9Å, the lattice constant of a primitive LSM (001) lattice.

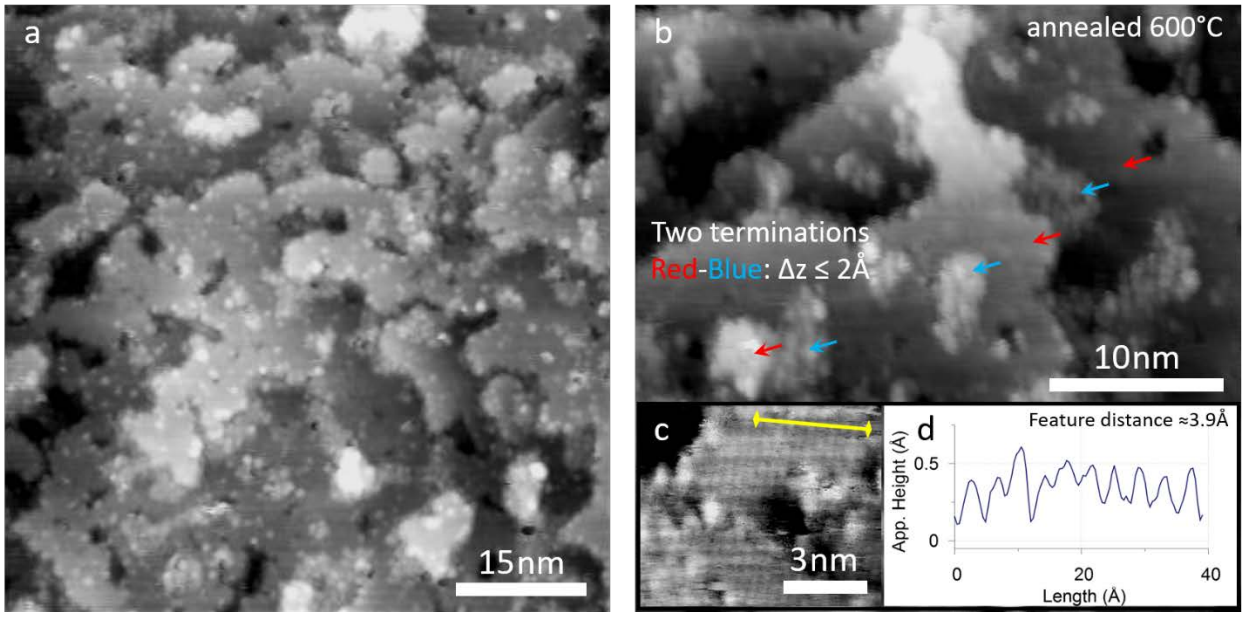

Figure 3-4. STM results of $La_{0.8}Sr_{0.2}MnO_3$(001), sputtered and annealed at 600°C in 2×10^{-5} mbar O_2. The surface is still rough but clean terraces are exposed. Two surface terminations coexist, indicated by the half-unit-cell step height (b). (c) Zoomed-in view of a terrace showing atomic rows, with a line scan (yellow line, graph in (d)) demonstrating that the feature distance matches the LSM unit cell size.

STM images acquired on an LSM (110) crystal present a similar picture to the (001) orientation. **Figure 3-5** shows a high density of steps with small terraces. However, in contrast to **Figure 3-3**, the surface appears to exhibit a preferential orientation, leading to an elongated shape of terraces. Moreover, the steps do not agglomerate, but assume an ordered, equidistant arrangement. The magnified image in the inset illustrates the structure on the terraces: rows with a spacing of approximately 7Å dominate the topography, highlighted by the white lines. The LEED pattern clearly demonstrates a rectangular surface unit cell. The lowest order spots (yellow rectangle) correspond to a periodicity of approximately 7.3Å, close to double the periodicity of a primitive surface unit cell (cyan rectangle).

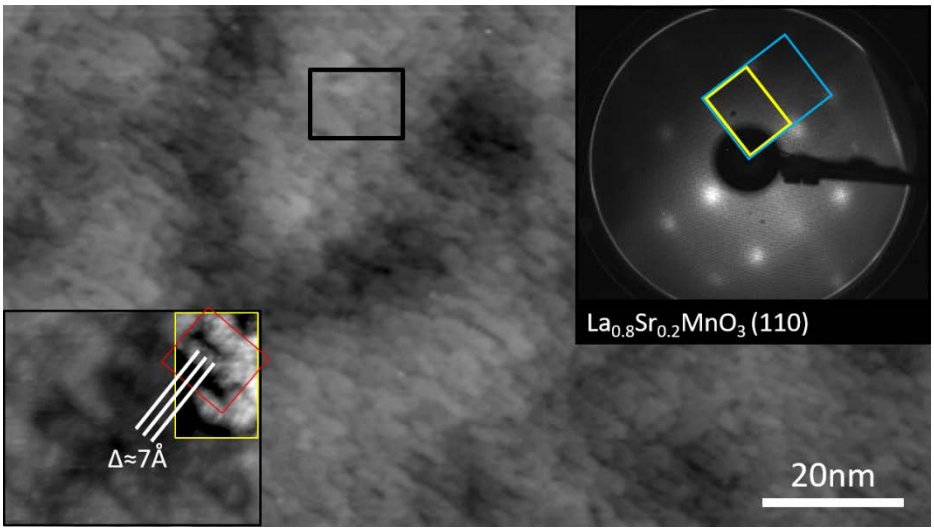

Figure 3-5. STM and LEED of $La_{0.8}Sr_{0.2}MnO_3$(110), sputtered and annealed at 735°C. The surface is characterized by a high density of steps with an elongated shape, indicating a preferential growth direction. The inset shows a magnified view of the region highlighted by the black box: row-like features with a distance of approximately 7Å are observed, indicating a surface reconstruction. The LEED pattern acquired at E_e = 45 eV shows a rectangular unit cell (yellow), which is approximately double the size of the primitive (blue) surface unit cell.

3.3. Extended X-ray absorption fine structure (EXAFS) measurement on LSM thin films

The structure of LSM and the coordination environment of its constituents have been studied using extended x-ray absorption fine structure measurements. In order to obtain surface-sensitive information the study was performed at grazing incidence so that only the evanescent field of the totally reflected x-ray beam interacts with LSM. Here, we present a comparison of four different preparations of LSM thin films on YSZ: as-prepared, annealed at 750°C in O_2, after deposition of 4Å Hf, and annealed at 750°C in O_2 after Hf deposition. **Figure 3-6** shows an overview of Sr K-edge EXAFS results for these four preparations. The intensity is plotted as a function of radial distance from the Sr site, corresponding to a Fourier-transformation of the raw data, measured as a function of photon energy. The main peaks corresponding to scattering sites within the LSM film are assigned as the respective nearest-neighbor bonding partners of the Sr cations. While the variations in the oxygen and manganese peaks are very small, substantial changes are occurring at distances exceeding the maximum of the Sr-Mn peak. With annealing, the profile of the Sr-La peak is flattened, potentially indicating the emergence of a different species. The deposition of Hf, on the other hand, appears to cause modifications at distances close to 4Å. The broadening in the La-Sr region upon annealing is also observed in the presence of Hf. In this case, however, part of the intensity shifts towards higher distances.

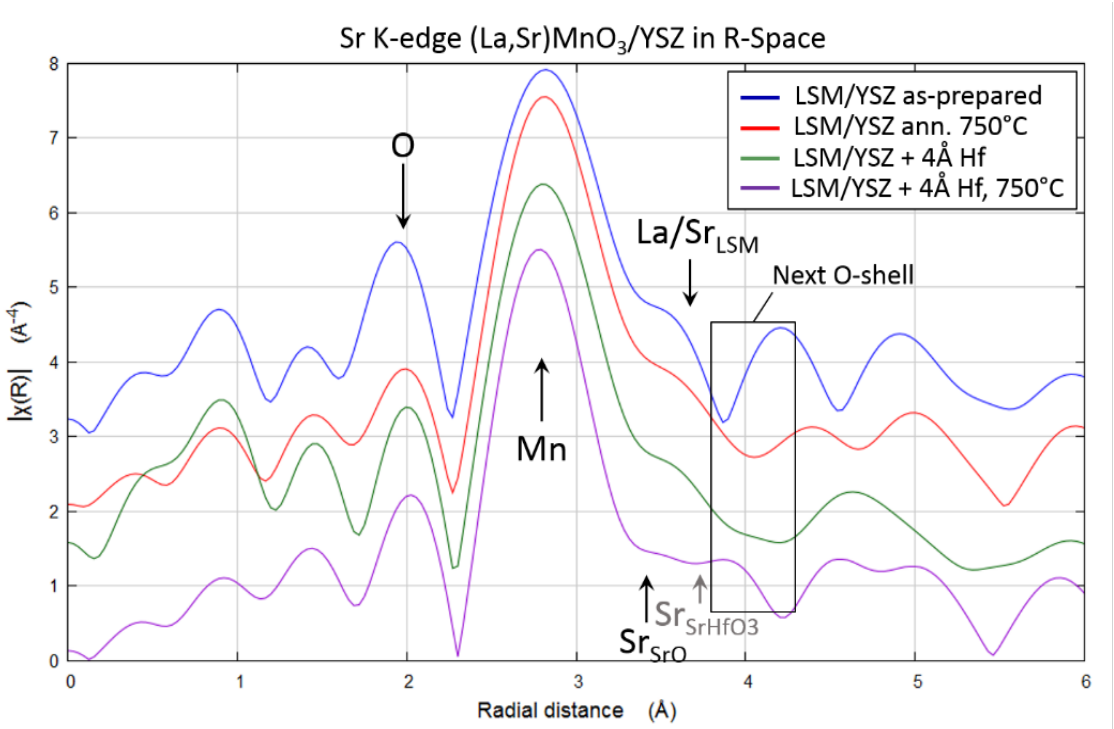

Figure 3-6. Extended x-ray absorption fine structure spectra of $La_{0.8}Sr_{0.2}MnO_3$ thin films, comparing different preparations: as-prepared, annealed at 750°C in O_2, as-prepared + 4Å Hf, annealed at 750°C in O_2 after depositing 4Å Hf.

3.4. Further discussion

The structure of both LSM and the species resulting from Sr segregation is an important topic of the present project. In order to learn about the nature and structure of the SrO_x species the coordination and bonding environment of Sr was analyzed using surface-sensitive EXAFS of as-grown and annealed LSM. While the peaks corresponding to the first two coordination shells (O and Mn) do not undergo any significant changes, the broadening of a peak close to 4Å is observed. This distance approximately corresponds to the Sr-Sr (and Sr-La) bond length, which is expected to undergo changes with the formation of a different phase containing Sr. The peak broadening towards lower bond lengths would be in agreement with a SrO-type structure, but the resolution in the spectra is not sufficient to draw valid conclusions.

In a second part of the EXAFS study, the effect of Hf deposition was investigated. While the room-temperature spectrum resembles the one of as-grown LSM, an even stronger broadening than for undoped LSM is observed after annealing Hf-doped LSM, indicating an additional bonding environment of Sr, potentially originating from a distortion of the surface region by Hf incorporation. A detailed, reliable analysis of the spectra is however challenging for all the EXAFS results presented here, since the observations are limited to peak broadening and intensity shifts rather than the emergence or suppression of clear separate peaks.

The atomic-scale surface properties of LSM have been studied on LSM (110) and (001) single crystals and thin films on $SrTiO_3$(001). Large-scale STM images show flat surfaces for LSM thin films on STO (**Figure 3-1**), which nevertheless exhibit a high density of islands, indicating a tendency of LSM to form steps. While the properties of thin films are influenced by the structure of the substrate, the preference for creating steps finds stronger resonance on LSM single crystals, for which the surfaces were found to be ordered, but rough (**Figures 3-3**, **3-4**, and **3-5**). The square arrangement of atoms observed on LSM/STO (001) (**Figure 3-2**) is generally in good agreement with the main termination observed on LSM (001) crystals after annealing in 2×10^{-5} mbar O_2. There, a row-like structure in agreement with the unit cell size of LSM (001) coexists with a second termination with terraces at a step size of 2Å, corresponding to half a cubic LSM unit cell, indicating a potential MnO_2-layer-based termination. Moreover, this termination is expected to be reconstructed, based on its row distance of at least twice the primitive unit cell. However, these terraces are small and appear highly disordered, indicating low stability and potential coexistence of different surface terminations. It should also be mentioned that we do not expect a row-based structure terminating the LSM (001) single crystals just based on the row-like structure of the main termination, which is assumed to be a La/Sr-O-based layer, based on the tendency of A-site surface enrichment. The observation of rows could certainly correspond to a square unit cell imaged with a slightly asymmetric STM tip, giving a square unit cell a row-like character. The high-resolution STM image of LSM (110) (**Figure 3-5**) shows rows of surface features with a spacing of approximately 7Å, which indicates the existence of a (2×1) surface reconstruction.

Corresponding trends are also observed in LEED measurements: patterns of LSM thin films exhibit sharp diffraction spots, based on the flatter and better-defined surface layers, whereas the features for the single crystal surfaces are weaker and broader. This broadening of diffraction spots is a result of both, the coexisting terminations for LSM (001) and the small terrace sizes observed in STM, approaching the coherence length of the electron beam. The LEED results for all three types of samples contain additional diffraction spots compared to the pattern expected for primitive LSM surface unit cells. While the measured LEED patterns do not allow for definite conclusions on the surface structure, the additional spots clearly demonstrate the presence of a surface reconstruction. Both observations, the tendency to form steps and the existence of surface reconstructions, indicate a high surface energy of bulk-terminated LSM, or the coexistence of terminations of similar energy. It further shows that different surface structures and terminations should be taken into account in the interpretation of surface processes on LSM.

4) Reversibility of dopant segregation

4.1. Dopant segregation is reversible with electrical polarization

First, polarization-segregation graph of LCM was obtained which is to be used as a reference for studying its activation behavior. For the experiments, aforementioned lateral polarization

method[40,70] was employed in order to minimize potential experimental artifacts. LCM films were annealed at 770˚C for 1h under several polarization values, -0.45, -0.3, -0.15, 0.3, 0.6, and 0.9V (circles in **Figure 4-1a**), and the resulting dopant segregation on each polarization was analyzed with X-ray photoelectron spectroscopy (XPS). The deconvolution of Ca 2*p* core-level spectrum into the surface (Ca_{surf}) and lattice component (Ca_{latt}) allowed the quantification of surface CaO_x-like phase which was formed as a result of Ca segregation (the same method as part 1)). The amount of Ca_{surf} normalized by (La+Ca) is plotted with respect to polarization as shown in **Figure 4-1b** (circles), re-confirming our previous results on LCM; Ca_{surf} monotonically decreases as polarization increases. To test the reversibility of Ca segregation, we annealed another batch of LCM film under two-step polarization where the polarization value changed from cathodic (1h) to anodic (1h); -0.45V → 0.9V, -0.3V → 0.6V, and -0.15V → 0.3V (triangles in **Figure 4-1a**). The amount of Ca_{surf} on each sample is plotted together with the segregation graph of LCM (triangles in **Figure 4-1b**), indicating that Ca segregation induced under cathodic polarization can be removed/reversed by applying anodic polarization.

To further confirm the result, the reversibility of Sr segregation on $La_{0.8}Sr_{0.2}MnO_3$ (LSM) was also tested with the similar method. LSM films were firstly annealed at 770˚C for 1h under several polarization values, -0.45, -0.3, -0.15, 0.2, 0.5, and 0.8V and their polarization histories are indicated as circles in **Figure 4-1c**. In accordance with our recent finding, it showed valley-shaped segregation behavior with respect to polarization (circles in **Figure 4-1d**) where segregation was minimum around 0 ~ 0.2V (V_{min}). To test the reversibility of Sr segregation, we compared this result with samples annealed under two-step polarizations. For testing cathodic activation, the polarization values were changed from anodic (1h) to V_{min} (1h); 0.8V → 0.15V, 0.5V → 0.1V, and 0.2V → 0.05V. For anodic activation, the changes were from cathodic (1h) to V_{min} (1h); -0.45V → 0.15V, -0.3V → 0.1V, and -0.15V → 0.05V. The polarization histories are indicated as triangles in **Figure 4-1c**. As a result, the final amount of segregation, indicated as triangles in **Figure 4-1d**, well followed the segregation graph of LSM after both cathodic and anodic activation processes.

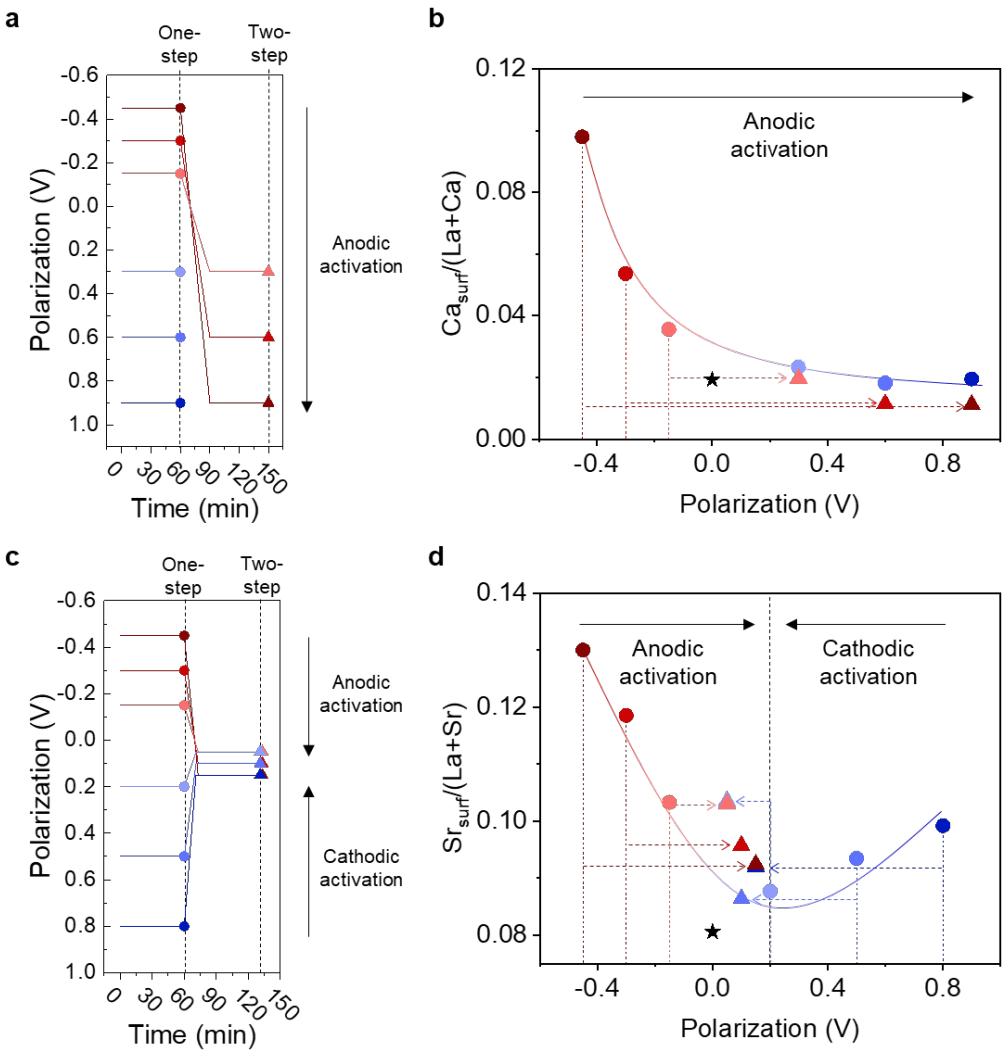

Figure 4-1. Reversibility of dopant segregation with polarization. **a**, $La_{0.8}Ca_{0.2}MnO_3$ thin films were annealed with lateral polarization method at 770˚C in pure pO_2 for 1h. First set of samples were annealed under -0.45, -0.3, -0.15, 0.3, 0.6, and 0.9V (circles). Another set of samples were annealed under two-step polarizations, -0.15V (1h) → 0.3V (1h), -0.3V (1h) → 0.6V (1h), and -0.45V (1h) → 0.6V (1h) (triangles). **b**, The amount of Ca segregation on each film was calculated by deconvoluting Ca 2*p* XPS spectra into Ca_{surf} and Ca_{latt}, and normalizing Ca_{surf} with total A-site cations, $Ca_{surf}/(La+Ca)$. The color and shape of each data point represent its polarization history shown in **a**. Star indicates the segregation amount on the as-prepared film. **c**, $La_{0.8}Sr_{0.2}MnO_3$ thin films were tested with the similar method. First set of films were annealed under single-step polarization; -0.45, -0.3, -0.15, 0.2, 0.5, and 0.8V (circles). Another set of samples were annealed under two-step (triangles) polarizations. For cathodic activation, the polarization values changed from anodic (1h) to V_{min} (1h); 0.8V → 0.15V, 0.5V → 0.1V, and 0.2V → 0.05V. For anodic activation, the changes were from cathodic (1h) to V_{min} (1h); -0.45V → 0.15V, -0.3V → 0.1V, and -0.15V → 0.05V. Resulting Sr segregation, $Sr_{surf}/(La+Sr)$, on each film was quantified by XPS and plotted with respect to the applied polarization.

4.2. Activation of LCM mediated by removing Ca segregation under anodic polarization

To investigate if the removal of dopant oxide at the LCM surface would lead to the activation of its oxygen exchange kinetics, we measured *in-situ* electrochemical impedance spectroscopy (EIS) while cycling the polarization between -0.15V and 0.9V under 1 atm O_2 at 770˚C. Each polarization value was chosen to induce segregation and redissolution of Ca, respectively, referring to **Figure 4-1b**. Please note that the lateral polarization method is no longer used and single polarizations were applied to the whole electrodes for the polarization experiments shown from now. As expected, applying -0.15V on LCM for 10 h increased the impedance of the cell markedly up to 2.6-fold (**Figure 4-2a**). The resulting EIS spectra consist of two semicircles at intermediate (~500 Hz) and low frequency (~20 Hz). Based on the previous EIS studies, each of them is attributed to the surface oxygen exchange reaction ($O_2 + 4e^- \leftrightarrow 2O^{2-}$) taking place at the grain boundary (R_{gb}) and grain surface (R_{gs}) of LCM, respectively[37,55,58,71,72]. Detailed explanations on the interpretation and fitting of EIS spectra are available in the Supporting Information. Interestingly, when 0.9V was applied thereafter, the EIS spectrum shrank rapidly in 5min and the impedance returned back to the similar value to the as-prepared sample after 30 min, thus confirming anodic activation. Such impedance change under different polarizations coincides well with the reversible segregation on LCM shown in **Figure 4-1b**; applying anodic polarization removes Ca segregation. Also, the impedance changes between -0.15V and 0.9V were reversible during several polarization cycles as can be seen in **Figure 4-2b**. Thus, these results confirm that anodic polarization can activate the surface of LCM and is mediated by removing Ca segregation.

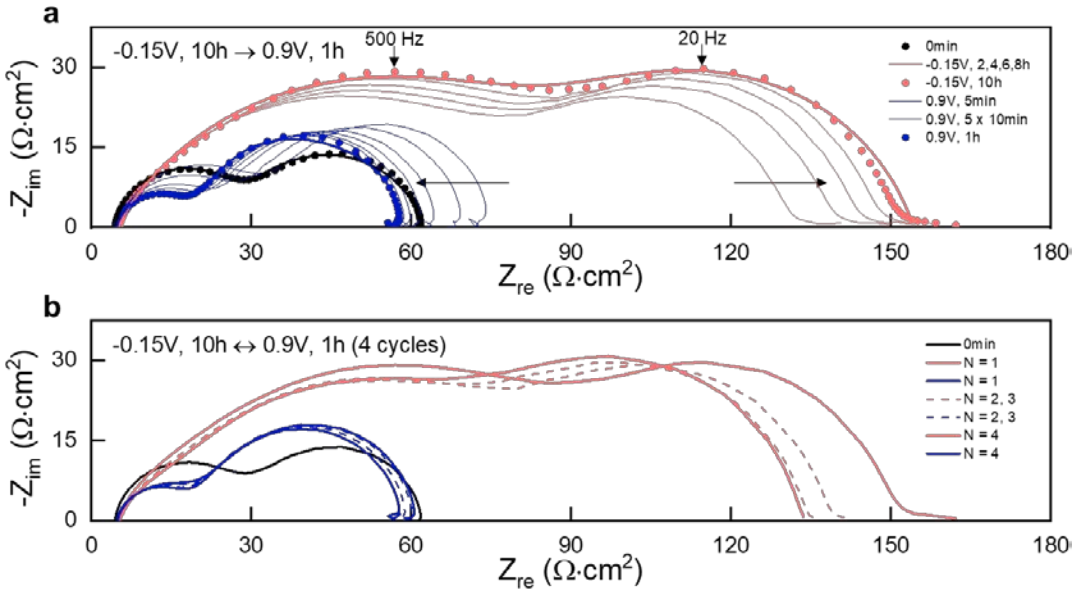

Figure 4-2. Rapid and reversible activation behavior of LCM under anodic polarization. All the *In-situ* EIS spectra were taken under 0V DC bias right after annealing LCM at 770˚C in 1 atm pO_2 under different polarizations for different time durations. **a**, LCM thin film was annealed under -0.15V for 10h, followed by annealing under 0.9V for 1h. EIS spectra were measured every 2h for

-0.15V and 10min for 0.9V. The polarization was switched with a ramping rate of 1mV/s. **b**, The polarization cycle between -0.15V (10h) and 0.9V (1h) was repeated 4 times.

4.3. Kinetics in reversing Ca segregation and activation

For more detailed study, we studied the kinetics in the reversibility of Ca segregation and anodic activation in a wide range of polarization. Several LCM films were annealed under cathodic polarization for 1h, followed by applying anodic polarization for different time durations. Then, the amount of CaO_x on each sample was quantified by XPS and plotted with respect to the time we applied anodic polarization. Two different cathodic polarizations, -0.15V and -0.6V, were chosen to vary the amount of dopant segregation before applying anodic polarization. **Figure 4-3a** shows the results from the samples that were annealed firstly under -0.15V and -0.6V, followed by annealing under anodic polarization. When dopant segregation was firstly induced under -0.15V, about half of the surface dopant oxide was removed within 5min after applying anodic polarizations (pink data points, please read the pink y-axis at the left side). Also, applying 0.9V (pink triangles) removed more dopant oxides than 0.3V (pink circles). The XPS results are further supported by scanning electron microscopy (SEM) images measured on each sample (**Figure 4-3b**, **4-3c**, and **4-3d**). The number of CaO_x surface particles decreased with the time duration of applying 0.9V and the surface of LCM started to show grainy structure (inset of **Figure 4-3d**) which is similar with that of the as-prepared sampl. Next, the effect of higher cathodic polarization, -0.6V, was studied (brown data points, please read the brown y-axis at the right side). As a result, about 2.8-times more CaO_x was formed at the surface of LCM than that of -0.15V-annealed sample (pink star *vs.* brown star in **Figure 4-3a**). This coincides well with the segregation graph of LCM in **Figure 4-1b**. Interestingly, very different kinetics in reversing Ca segregation was observed when the films were annealed under -0.6V. Comparison between pink and brown data points in **Figure 4-3a** reveals that dopant oxides were removed in a much slower rate when Ca segregation was induced under higher cathodic polarization. The initial rate of reversing segregation for -0.15V → 0.9V was $-7.7h^{-1}$ while that of -0.6V → 0.9V was only $-0.12h^{-1}$. Regarding its surface morphology, Ca did not precipitate as particles under -0.6V [70] (**Figure 4-3e**), unlike the case of -0.15V in **Figure 4-3b**. However, the grainy structure again started to evolve on the LCM surface after applying anodic polarizations (**Figure 4-3g**).

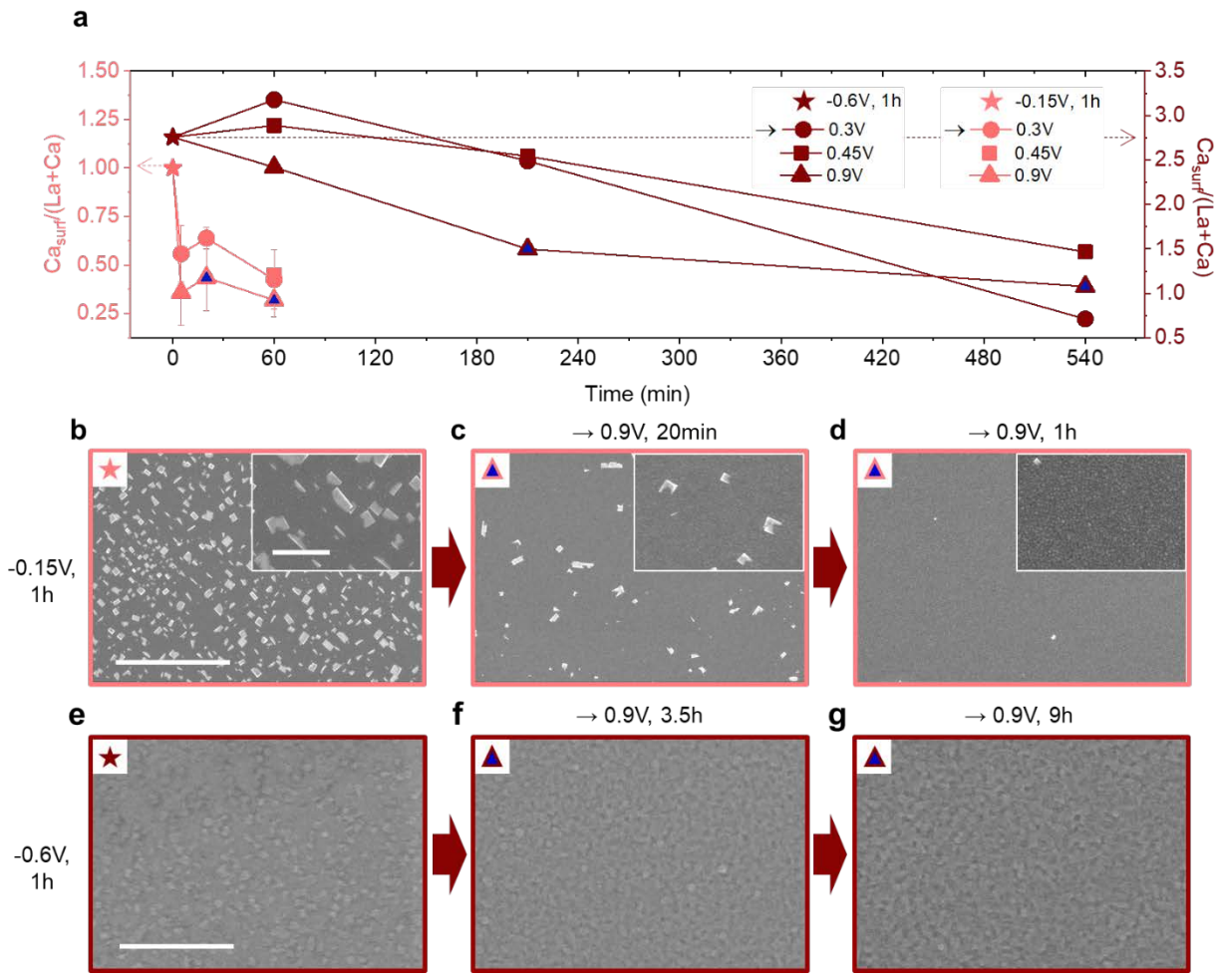

Figure 4-3. Kinetics in reversing Ca segregation and corresponding surface morphologies of LCM. **a**, LCM thin films were annealed under two-step polarizations at 770˚C in 1 atm pO_2, and the resulting amount of CaO_x on each sample was quantified by deconvoluting its Ca 2*p* XPS spectra and plotted with respect to the time duration of applying anodic polarizations. Cathodic polarizations were first applied for 1h to induce Ca segregation; -0.15V (pink star, please read the y-axis at the left side) and -0.6V (brown star, please read the y-axis at the right side). Then, different anodic polarizations were applied for different time periods to remove Ca segregation; 0.3V (circles), 0.45V (squares), and 0.9V (triangles). The SEM images were taken on the samples annealed under -0.15V → 0.9V (**b**, **c**, and **d**) and -0.6V → 0.9V (**e**, **f**, and **g**). Mark at the top-left corner of each image represents the corresponding data point in **a**. Scale bars in **b** and **e** represent 4 μm and one in the right inset of **b** indicates 800 nm.

We then investigated the corresponding activation processes at different times for comparison with the kinetics of reversing Ca segregation assessed above. To do this, EIS measurements were performed on LCM films under the same conditions we used for the above segregation study. As -0.15V was applied to LCM film, the impedance of the cell continuously increased as can be seen in **Figure 4-4**, which coincides well with the formation of insulating CaO_x evidenced by XPS and

SEM results in **Figure 4-3a** and **4-3b**. After applying -0.15V for 1h, anodic polarization was applied to remove CaO_x and the total impedance of the cell was measured over time. The resulting total impedances at different times were normalized (Z_{norm}) and plotted in **Figure 4-5a** (deep pink data points, please read the thick y-axis at the left side). The graph shows that Z_{norm} shrink very fast close to the initial low value (Z_{norm} = 0 when $Z_{anodic} = Z_{initial}$) within a few minutes and 0.9V (deep pink triangles) was more efficient for activation than 0.3V (deep pink circles). On the other hand, when LCM film was passivated under -0.6V, followed by activation under 0.3V (deep brown circles), the total impedance decreased in a far slower rate than the -0.15V case and it could not fully recover the initial impedance even after 10h. For a comparison of the activation processes with the kinetics of Ca segregation, the amounts of Ca_{surf} at different times are plotted together in **Figure 4-5a** (light data points, please read the thin y-axis at the right side). It can be seen that the time took for removing Ca_{surf} and activating LCM followed the same trend; -0.15V → 0.9V < -0.15V → 0.3V << -0.6V → 0.3V. Also, the final impedances and amounts of CaO_x followed the same order; 0.15V → 0.9V < -0.15V → 0.3V < -0.6V → 0.3V. Above results further confirm that redissolution of CaO_x under anodic polarization induced activation and that activation kinetics is affected by the initial cathodic polarization value on the LCM film.

Next, the reversibility of activation and passivation process is assessed. Each polarization cycle, -0.15V ↔ 0.9V, -0.15V ↔ 0.3V, and -0.6V ↔ 0.3V, was repeated four or five times and the resulting impedance changes are shown in **Figure 4-5b**, **4-5c**, and **4-5d**, respectively. In all the polarization cycles, the changes were very reversible in terms of both the shape and magnitude of EIS spectra. Also, SEM images of each film showed that there were no significant microstructural changes. In some cases, however, the EIS spectra were not reversible. **Figure 4-6** shows irreversible change of EIS spectrum after finishing the first polarization cycle between -0.6V (1h) ↔ 0.9V (10h). According to the previous studies on LSM thin film, microcracks or holes were formed when a high anodic polarization was applied to the film and sometimes this led to slight decrease in the impedance of the film by making new current pathways [37,73,74]. Likewise, we could also observe the formation of microcracks or delamination of the LCM film when high anodic polarization (0.9V) was applied for a long time (10h) as can be seen in **Figure 4-6**. Such microstructural changes caused permanent decrease in R_{gb}, resulting in irreversible EIS spectra between polarization cycles.

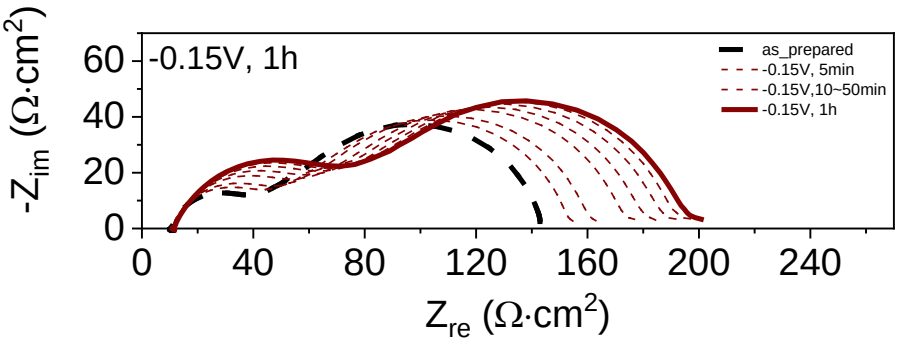

Figure 4-4. EIS spectra were obtained at 770˚C in 1 atm pO_2 while applying -0.15V on LCM for 5, 10, 20, 30, 40, 50, and 60 min.

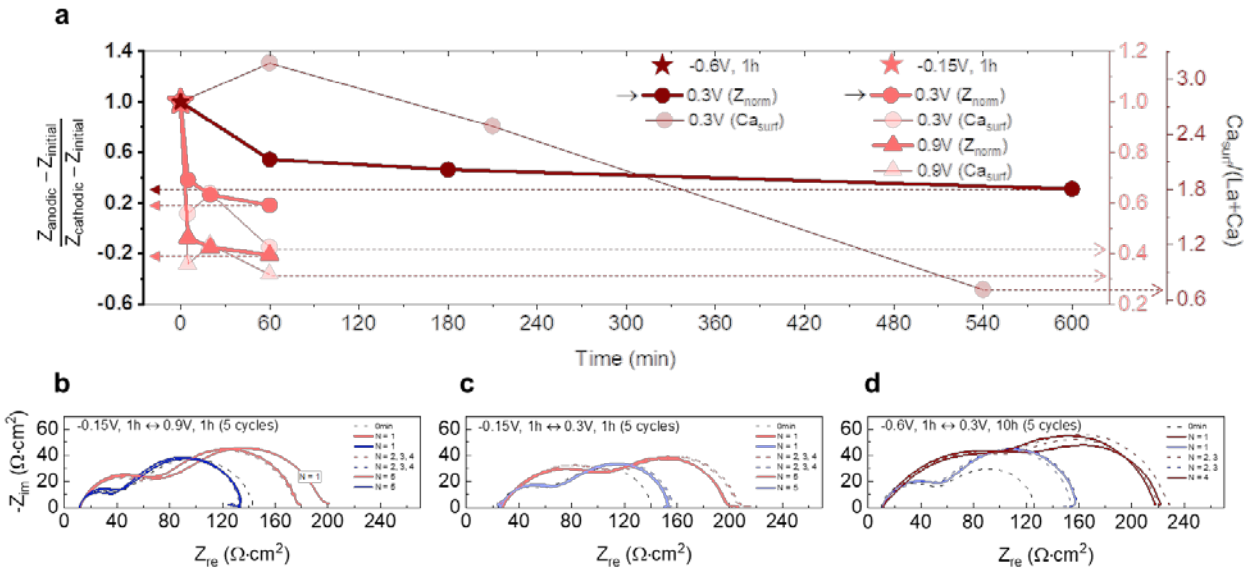

Figure 4-5. Kinetics in the anodic activation of LCM and its correlation with the reversibility of Ca segregation. **a**, After applying cathodic polarizations on LCM thin films for 1h, EIS spectra were obtained at 770˚C in 1 atm pO_2 while applying anodic polarizations. The resulting total impedance values were normalized by $Z_{normalized} = (Z_{anodic} - Z_{initial})/(Z_{cathodic} - Z_{initial})$; $Z_{normalized} = 0$ when $Z_{anodic} = Z_{initial}$ and $Z_{normalized} = 1$ when $Z_{anodic} = Z_{cathodic}$ (indicated as stars). The resulting values are plotted with respect to the time period of applying anodic polarizations (please read the thick y-axis at the left side); 0.15V (1h) → 0.3V (deep pink circles), 0.15V (1h) → 0.9V (deep pink triangles), and 0.6V (1h) → 0.3V (deep brown circles). For comparison, the amount of Ca_{surf} is plotted together with light colors (please read the thin y-axis at the right side). To test the reversibility of anodic activation, each polarization cycle was repeated four or five times; **b**, -0.15V (1h) ↔ 0.9V (1h), **c**, -0.15V (1h) ↔ 0.3V (1h), and **d**, -0.6V (1h) ↔ 0.3V (10h).

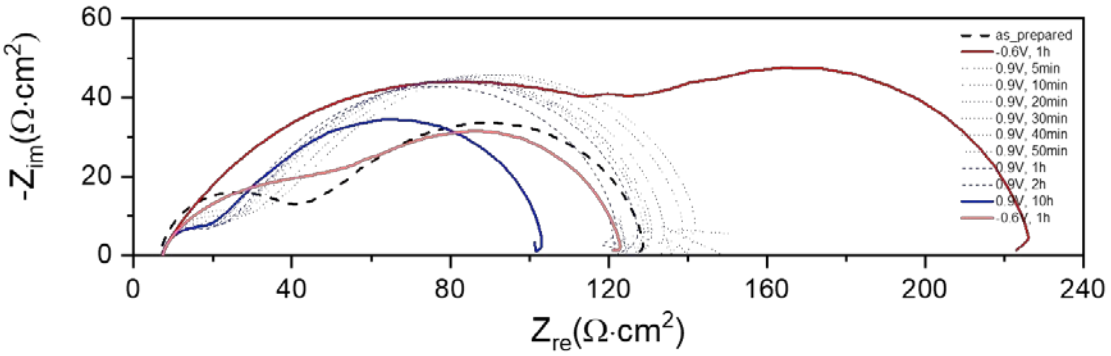

Figure 4-6. After applying -0.6V on LCM at 770˚C in 1 atm pO_2 for 1h, EIS spectra were obtained while applying 0.9V for different time periods.

4.4. A novel mechanism behind anodic activation

We have confirmed experimentally that anodic activation is possible by electrochemically modifying the chemistry of perovskite oxides toward the point where driving force (E_{elec}) of Ca segregation is suppressed. However, it should be noted that modifying the chemistry of perovskite oxides does not necessarily lead to the dissolution of 'secondary' phases into the perovskite oxides. Previously proposed mechanism that explains the redissolution of SrO into LSM under cathodic polarization (equation (1)) cannot explain our results under anodic polarization.

$$V_{La}''' + SrO_{surf} + 2Mn_{Mn}^{X} \rightarrow Sr_{La}' + 2Mn_{Mn}'' + 1/2O_2 \quad (1)$$

Equation (1) explains that LSM incorporates Sr of SrO_{surf} into its A-site vacancy while it is being reduced under cathodic polarization, and *vice versa* under anodic polarization. However, our result was the opposite of this; CaO was removed under anodic polarization. To reveal the mechanism of anodic activation, we measured X-ray absorption spectroscopy (XAS) on the LCM films that we used for the segregation study in **Figure 4-3a**.

Figure 4-7a and **4-7b** show the O *K*-edge XAS spectrum of the samples measured in total-electron-yield (TEY) mode. In general, the first peak at ~530 eV is attributed to hybridized Mn 3*d*–O 2*p* state (h_{3d}), and the second (~536 eV) and third peaks (~544 eV) correspond to La 5*d*–O 2*p* and Mn 4*sp*–O 2*p* states, respectively [75-78]. Especially, the integrated area of the first peak at ~530 eV can be employed to assess the valence state of perovskite oxides. The area of this peak increases with oxidation of the sample as electrons in the h_{3d} state near the Fermi level are removed. For the samples annealed firstly under -0.15V, the h_{3d} peak showed an abrupt increase in its intensity after applying 0.9V just for 5min and retained the same intensity afterwards (**Figure 4-7a**). On the other hand, when the samples were annealed firstly under -0.6V, the h_{3d} peak increased very slowly under the same 0.9V polarization and continued to increase during 9h (**Figure 4-7b**). Possible contributions from the formation of other oxides, such as CaO, La_2O_3, and MnO_x, to the increase in h_{3d} peak were confirmed to be negligible [79-81]. Our result coincides with a previous paper by Mizusaki *et al.* [82] where they predicted non-bonding O 2*p* state being redox-active when LSM has oxygen-excess defect chemistry under high pO_2 regime (**Figure 4-7d**). Thus, based on the changes in the O *K*-edge of the two set of samples, it can be concluded that the samples polarized firstly under -0.6V underwent much slower oxidation process upon annealing under 0.9V than the -0.15V ones. We then plotted the integrated area of h_{3d} peaks in the O *K*-edge spectra with respect to the time duration of applying 0.9V (deep triangles in **Figure 4-7c**) and compared the resulting graphs with the temporal changes in the amount of CaO_x (light triangles in **Figure 4-7c**) shown in **Figure 4-3a**. Interestingly, the temporal changes of CaO_x and the change in the oxidation state of LCM were in a reverse relationship between each other (note that y-axis at the left side increases in a reverse direction). This is a clear indicator that oxidation process occurring at the surface of LCM under anodic polarization promoted the removal of CaO_x, and thus activation.

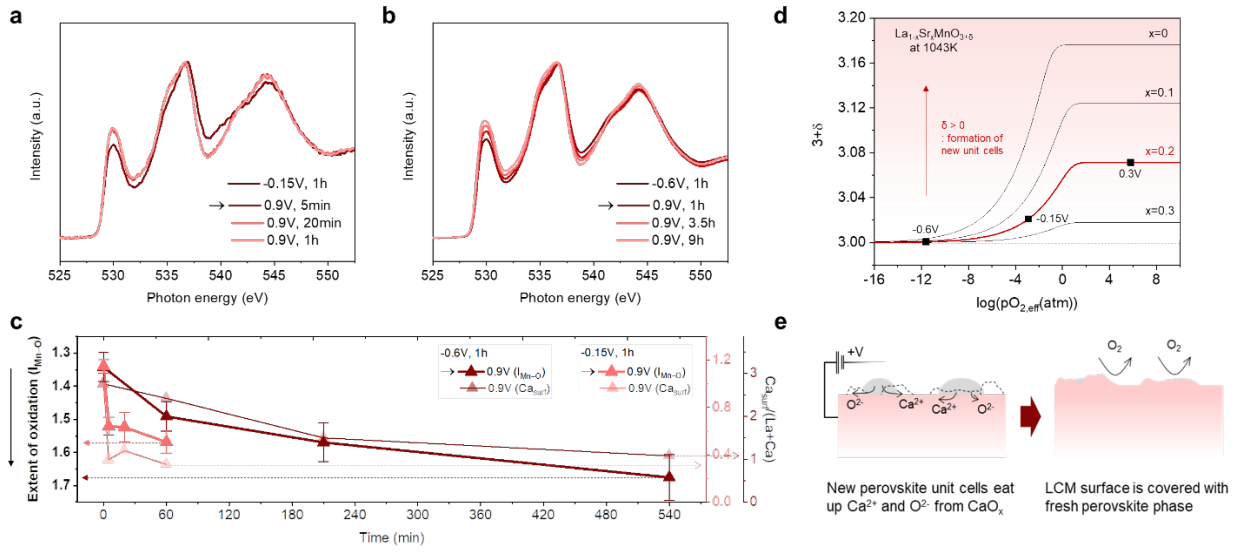

Figure 4-7. Oxygen-excess non-stoichiometry of LCM coupled with a formation of new fresh unit cell reactivates its surface. **a**, Total-electron-yield O *K*-edge XAS spectra measured on LCM thin films after annealing under -0.15V, followed by annealing under 0.9V for 5min, 20min, and 1h. **b**, Another set of samples were annealed under -0.6V, followed by annealing under 0.9V for 1h, 3.5h, and 9h. **c**, The area of Mn 3*d*–O 2*p* peaks in each O *K*-edge XAS spectra is integrated and plotted with respect to the time we applied anodic polarization (please read the thick y-axis at the left side). Deep pink triangles indicate the samples initially annealed at -0.15V for 1h and deep brown triangles represent those annealed at -0.6V for 1h. For comparison, the amount of Ca_{surf} is plotted together with light colors (please read the thin y-axis at the right side). **d**, Oxygen-excess non-stoichiometry of $La_{1-x}Sr_xMnO_{3+\delta}$ (x=0, 0.1, 0.2, and 0.3) with respect to effective pO_2 (replotted from a previous work by Mizusaki *et al.* [82]). The curve that coincides with the composition of our LCM is colored in red and the anodic polarization values we used are converted to the corresponding $pO_{2,eff}$ according to Nernst equation (marked as squares). **e**, Schematics describing the mechanism of activation process on LCM under anodic polarization.

Importantly, this result could explain the reason that LCM samples firstly annealed under -0.6V took far more time for activation than those annealed under -0.15V (**Figure 4-3a** and **4-5a**). According to the defect chemistry of LSM [82], LCM would also depleted with V_{La}''' and V_{Mn}''' as it being reduced under -0.6V, given that it represented similar defect chemistry with LSM. In contrast, the one passivated under -0.15V would have a fairly high amount of V_{La}''' and V_{Mn}'''. As oxidation of lanthanum manganites accompanies a migration of A- and B-site cations (detailed explanation is given in the next paragraph), different amount of cation vacancies would result in different oxidation rates of LCM film and thus different activation speed.

All the results shown so far boil down to one important conclusion: oxidation process of LCM surface induces dissolution of insulating CaO_x and activates the oxygen exchange reaction. We then investigated possible defect reactions that can explain this. First, we recognized that different defect equation from equation (1) should be used for describing the defect chemistry

of perovskite oxide under anodic polarization. Basically, due to its close-packed structure, perovskite oxide forms cation vacancies under oxidizing condition to satisfy oxygen-excess non-stoichiometry ($A_{1-\lambda}B_{1-\lambda}O_3 = ABO_{3+\delta}$) instead of incorporating oxygen at its interstitial sites [83,84]. Corresponding defect reaction of lanthanum manganite under oxidation is written as:

$$nil + 6Mn_B^x + 3/2O_2 = V_{La}''' + V_{Mn}''' + 6Mn_B^{\cdot} + 3O_O^x \quad (2)$$

Or, can be rewritten as [82]:

$$LaMnO_3 + \frac{\delta}{2}O_2 = (La\square_{\delta/3})(Mn\square_{\delta/3})O_{3+\delta} = \frac{3+\delta}{3}\{(La_{3/(3+\delta)}\square_{\delta/(3+\delta)})(Mn_{3/(3+\delta)}\square_{\delta/(3+\delta)})O_3\} \quad (3)$$

Equation (2) and (3) describe that new perovskite unit cells with a stoichiometric amount of $\frac{\delta}{3}$ are formed at the surface of perovskite oxide by incorporating oxygen and forming cation vacancies in the bulk during its oxidation. Dopant and the possibility of dominant V_{La}''' formation over V_{Mn}''' [82] are not considered in this equation just for simplicity. Also, previous HR-TEM measurement on $LaMnO_{3+\delta}$ showed that there was no formation of secondary species during the process [85]. Mizusaki *et al.* previously formulated the oxygen-excess defect chemistry of LSM [82] and we replotted the curves in **Figure 4-7d**, considering our experimental conditions (see Supporting Information for the details). It is noteworthy that the amount of dopant is critical for the oxygen-excess non-stoichiometry (δ); higher amount of dopant suppresses the formation of new unit cells $\left(\frac{\delta}{3}\right)$. The curve that represents the composition of our LCM ($La_{0.8}Ca_{0.2}MnO_3$) is highlighted in red, and different polarization values, -0.6, -0.15, and 0.3V, are converted to the corresponding hypothetical $pO_{2,eff}$ and marked as squares.

Inspired from the fact that oxidation process occurring at the surface of LCM induces the anodic activation, we propose that the formation of new unit cells under anodic polarization would draw Ca^{2+} and O^{2-} out of CaO_x at the surface and incorporate them into the A-site and O-site of the new unit cells, respectively (**Figure 4-7e**). This is possible because Ca^{2+} and O^{2-} are readily enriched at the surface which could be directly used for forming new lattices. Also, the fact that there is a maximum in the number of new lattices $\left(\frac{\delta}{3}\right)$ as shown in **Figure 4-7d** indicates that it would be better to change the operation mode before significant segregation occurs under SOFC mode. The reason that -0.6V-annealed sample could not recover its initial impedance even after quite a long time of anodic activation was most probably because the amount of Ca_{surf} was too much for the new lattices to fully incorporate them. We also think that suppressed driving force of Ca segregation, E_{elec}, under anodic polarization would facilitate this process by continuously pushing Ca from the near-surface region to the bulk of the perovskite phase. Modified from (2), the final defect reaction explaining this mechanism is shown as equation (4) with oxygen ions as redox-active species.

$$nil + CaO_{surf} + 2O_O^x + V_O^{\cdot\cdot} + 3/2O_2 \rightarrow Ca_{La}' + 6O_O^{\cdot} + V_{Mn}''' \quad (4)$$

Conclusion

The surface segregation of dopants in perovskite manganites under polarization has been investigated from several perspectives using XPS, EXAFS, LEED, STM, and AFM. Information on the surface structure of $La_{0.8}Sr_{0.2}MnO_3$ (001) and $La_{0.8}Sr_{0.2}MnO_3$ (110) surfaces has been obtained, as well as EXAFS data on the changes of the Sr bonding environment and the potential formation of new phases on LSM surface upon annealing. Different approaches to influence the electrostatic and elastic driving forces of segregation have been studied. While metal deposition has been employed to modify the reducibility of the surface of LSM and hence the electrostatic driving force of segregation, a systematic study of the polarization dependence of dopant segregation in $La_{0.8}Ca_{0.2}MnO_3$, $La_{0.8}Sr_{0.2}MnO_3$, and $La_{0.8}Ba_{0.2}MnO_3$ addresses both driving forces simultaneously. The deposition of Hf has been found to stabilize the surface of $La_{0.8}Sr_{0.2}MnO_3$ as a result of a decreased oxygen vacancy concentration, which reduces the electrostatic attraction of dopant cations to the surface. In the polarization-dependent study the oxygen vacancy concentration has been modified across a wide range, using both cathodic and anodic polarization. This approach allows for a systematic study of segregation as a function of effective oxygen pressures ranging from 10^{-16} to 10^{15} atm. The large variation of the oxygen chemical potential is expected to simultaneously affect the two main origins of segregation reported in the literature: the lattice mismatch of the dopant with the host cation La and the electrostatic attraction of the aliovalent dopants by a high oxygen vacancy density at the surface. The different dopant cation sizes in $La_{0.8}Ca_{0.2}MnO_3$, $La_{0.8}Sr_{0.2}MnO_3$, and $La_{0.8}Ba_{0.2}MnO_3$ exclusively affect the role of the elastic contribution. In all cases, a transition point between the two driving forces is observed for a characteristic oxygen pressure. Its dependence on the cation radii of the dopants ($R_{Ba} > R_{Sr} > R_{Ca}$) sheds light on the dominant origin of segregation at each point. The observation of a non-linear dependence of segregation on oxygen chemical potential provides context for the different observations in literature and illustrates the delicate balance of electrostatic and elastic energies. The reported observations systematically relate the surface degradation of perovskite electrode materials to oxygen pressure and polarization and help identify the dominant driving force of segregation at different conditions. Lastly, we have demonstrated that such degradation by dopant segregation can also be 'removed' by applying polarization. The applied polarization values were chosen to minimize the two driving forces of Sr and Ca segregation on LSM and LCM, respectively. We used LCM as a model system for specifically studying anodic activation process, and through a series of kinetics studies, we could finally propose the mechanism of anodic activation which had not been clarified before. This insight points toward the advantage of using perovskite oxides in a reversible mode between SOFC and SOEC, where once degraded LCM surface during SOFC operation can regain its original activity during SOEC operation. Also, it is worth noting that there are other perovskite oxides which show oxygen-excess non-stoichiometry[86], like lanthanum manganites we studied. We believe our finding would thus open new doors for activating various kinds of perovskite oxides in their applications.

Outlook

On the basis of the results presented above, we are concluding the studies of the polarization dependence of Sr segregation and the effect of Hf deposition on $La_{0.8}Sr_{0.2}MnO_3$ and will submit them for publication in the near future. The efforts to resolve the structure of SrO_x and the surface structure of $La_{0.8}Sr_{0.2}MnO_3$ will be intensified in year 3. Surface science studies will be performed on $La_{0.8}Sr_{0.2}MnO_3$ films on Nb:$SrTiO_3$ as well as on a new set of $La_{0.8}Sr_{0.2}MnO_3$(001) single crystals recently supplied by our collaborator Professor Joe Checkelsky at MIT. We aim to reproduce and improve the atomic-scale information on the surface structure and composition, as well as investigate the role of different preparation conditions for single crystal surfaces and growth conditions for thin film. Upcoming synchrotron beamtimes including EXAFS in October 2018 will provide an opportunity to reproduce the preliminary results reported here, improve the data quality and develop models for the structure of the segregated Sr species or the surface modifications resulting from metal deposition.

References

1 Singhal, S. C. Advances in solid oxide fuel cell technology. *Solid State Ionics* **135**, 305-313, doi:10.1016/S0167-2738(00)00452-5 (2000).

2 Singhal, S. C. & Kendall, K. *High-temperature solid oxide fuel cells: fundamentals, design and applications*. (Elsevier, 2003).

3 Gorte, R. J. & Vohs, J. M. Catalysis in Solid Oxide Fuel Cells. *Annual Review of Chemical and Biomolecular Engineering* **2**, 9-30, doi:10.1146/annurev-chembioeng-061010-114148 (2011).

4 Kuklja, M. M., Kotomin, E. A., Merkle, R., Mastrikov, Y. A. & Maier, J. Combined theoretical and experimental analysis of processes determining cathode performance in solid oxide fuel cells. *Physical Chemistry Chemical Physics* **15**, 5443-5471, doi:10.1039/C3CP44363A (2013).

5 Laguna-Bercero, M. A. Recent advances in high temperature electrolysis using solid oxide fuel cells: A review. *Journal of Power Sources* **203**, 4-16, doi:10.1016/j.jpowsour.2011.12.019 (2012).

6 Kilner, J. A. & Burriel, M. Materials for intermediate-temperature solid-oxide fuel cells. *Annual Review of Materials Research* **44**, 365-393, doi:10.1146/annurev-matsci-070813-113426 (2014).

7 Habib, M. A., Nemitallah, M. & Ben-Mansour, R. Recent Development in Oxy-Combustion Technology and Its Applications to Gas Turbine Combustors and ITM Reactors. *Energy & Fuels* **27**, 2-19, doi:10.1021/ef301266j (2013).

8 Adler, S. B., Lane, J. A. & Steele, B. C. H. Electrode Kinetics of Porous Mixed-Conducting Oxygen Electrodes. *Journal of The Electrochemical Society* **143**, 3554-3564, doi:10.1149/1.1837252 (1996).

9 Hauch, A., Jensen, S. H., Ramousse, S. & Mogensen, M. Performance and durability of solid oxide electrolysis cells. *Journal of The Electrochemical Society* **153**, A1741-A1747 (2006).

10 Waser, R. & Aono, M. Nanoionics-based resistive switching memories. *Nature Materials* **6**, 833-840, doi:10.1038/nmat2023 (2007).

11 Kilner, J., Berenov, A. & Rossiny, J. in *Perovskite Oxide for Solid Oxide Fuel Cells* 95-116 (Springer, 2009).

12 Mastrikov, Y. A., Merkle, R., Heifets, E., Kotomin, E. A. & Maier, J. Pathways for Oxygen Incorporation in Mixed Conducting Perovskites: A DFT-Based Mechanistic Analysis for (La, Sr)MnO3−δ. *The Journal of Physical Chemistry C* **114**, 3017-3027 (2010).

13 Adler, S. B. Factors Governing Oxygen Reduction in Solid Oxide Fuel Cell Cathodes. *Chemical Reviews* **104**, 4791-4844, doi:10.1021/cr020724o (2004).

14 Singhal, S. C. Solid Oxide Fuel Cells: Status, Challenges and Opportunities. *Advances in Science and Technology* **45**, 1837-1846, doi:10.4028/www.scientific.net/AST.45.1837 (2006).

15 Cai, Z., Kubicek, M., Fleig, J. & Yildiz, B. Chemical Heterogeneities on $La_{0.6}Sr_{0.4}CoO_{3-\delta}$ Thin Films—Correlations to Cathode Surface Activity and Stability. *Chemistry of Materials* **24**, 1116-1127, doi:10.1021/cm203501u (2012).

16 Kubicek, M., Limbeck, A., Frömling, T., Hutter, H. & Fleig, J. Relationship between Cation Segregation and the Electrochemical Oxygen Reduction Kinetics of $La_{0.6}Sr_{0.4}CoO_{3-\delta}$ Thin Film Electrodes. *Journal of The Electrochemical Society* **158**, B727-B734, doi:10.1149/1.3581114 (2011).

17 Druce, J. *et al.* Surface termination and subsurface restructuring of perovskite-based solid oxide electrode materials. *Energy & Environmental Science* **7**, 3593-3599, doi:10.1039/C4EE01497A (2014).

18 Rupp, G. M. *et al.* Correlating surface cation composition and thin film microstructure with the electrochemical performance of lanthanum strontium cobaltite (LSC) electrodes. *Journal of Materials Chemistry A* **2**, 7099-7108, doi:10.1039/C3TA15327D (2014).

19 Lee, W., Han, J. W., Chen, Y., Cai, Z. & Yildiz, B. Cation Size Mismatch and Charge Interactions Drive Dopant Segregation at the Surfaces of Manganite Perovskites. *Journal of the American Chemical Society* **135**, 7909-7925, doi:10.1021/ja3125349 (2013).

20 Porotnikova, N. M. *et al.* Effect of AO Segregation on Catalytical Activity of La0.7A0.3MnO3±δ (A = Ca, Sr, Ba) Regarding Oxygen Reduction Reaction. *Catalysis Letters*, doi:10.1007/s10562-018-2456-7 (2018).

21 Zuev, A. Y. & Tsvetkov, D. S. Oxygen nonstoichiometry, defect structure and defect-induced expansion of undoped perovskite LaMnO3±δ. *Solid State Ionics* **181**, 557-563, doi:https://doi.org/10.1016/j.ssi.2010.02.024 (2010).

22 Lee, W., Han, J. W., Chen, Y., Cai, Z. & Yildiz, B. Cation size mismatch and charge interactions drive dopant segregation at the surfaces of manganite perovskites. *Journal of the American Chemical Society* **135**, 7909-7925, doi:10.1021/ja3125349 (2013).

23 Saiful Islam, M. Ionic transport in ABO3 perovskite oxides: a computer modelling tour. *Journal of Materials Chemistry* **10**, 1027-1038, doi:10.1039/a908425h (2000).

24 Katsiev, K., Yildiz, B., Balasubramaniam, K. & Salvador, P. A. Electron tunneling characteristics on La0.7Sr0.3MnO3 thin-film surfaces at high temperature. *Applied Physics Letters* **95**, 092106, doi:10.1063/1.3204022 (2009).

25 Kubicek, M. *et al.* Cation diffusion in La(0.6)Sr(0.4)CoO(3-delta) below 800 degrees C and its relevance for Sr segregation. *Phys Chem Chem Phys* **16**, 2715-2726, doi:10.1039/c3cp51906f (2014).

26 Horita, T., Sakai, N., Kawada, T., Yokokawa, H. & Dokiya, M. Grain-Boundary Diffusion of Strontium in (La,Ca)CrO3 Perovskite-Type Oxide by SIMS. *Journal of the American Ceramic Society* **81**, 315-320, doi:doi:10.1111/j.1151-2916.1998.tb02336.x (1998).

27 Tsvetkov, N., Lu, Q., Sun, L., Crumlin, E. J. & Yildiz, B. Improved chemical and electrochemical stability of perovskite oxides with less reducible cations at the surface. *Nature Materials* **15**, 1010-1016, doi:10.1038/nmat4659 (2016).

28 Fister, T. T. *et al.* In situ characterization of strontium surface segregation in epitaxial $La_{0.7}Sr_{0.3}MnO_3$ thin films as a function of oxygen partial pressure. *Applied Physics Letters* **93**, 151904, doi:10.1063/1.2987731 (2008).

29 Crumlin, E. J. *et al.* In Situ Ambient Pressure X-ray Photoelectron Spectroscopy of Cobalt Perovskite Surfaces under Cathodic Polarization at High Temperatures. *The Journal of Physical Chemistry C* **117**, 16087-16094, doi:10.1021/jp4051963 (2013).

30 Mutoro, E. *et al.* Reversible Compositional Control of Oxide Surfaces by Electrochemical Potentials. *The Journal of Physical Chemistry Letters* **3**, 40-44, doi:10.1021/jz201523y (2012).

31 Baumann, F. S. *et al.* Strong Performance Improvement of $La_{0.6}Sr_{0.4}Co_{0.8}Fe_{0.2}O_{3-\delta}$ SOFC Cathodes by Electrochemical Activation. *Journal of The Electrochemical Society* **152**, A2074-A2079, doi:10.1149/1.2034529 (2005).

32 Ullmann, H., Trofimenko, N., Tietz, F., Stöver, D. & Ahmad-Khanlou, A. Correlation between thermal expansion and oxide ion transport in mixed conducting perovskite-type oxides for SOFC cathodes. *Solid State Ionics* **138**, 79-90, doi:10.1016/S0167-2738(00)00770-0 (2000).

33 Opitz, A. K. *et al.* Thin film cathodes in SOFC research: How to identify oxygen reduction pathways? *Journal of Materials Research* **28**, 2085-2105, doi:DOI: 10.1557/jmr.2013.216 (2013).

34 Traulsen, M. L., de Carvalho, H. W. P., Zielke, P. & Grunwaldt, J.-D. The Effect of Electrical Polarization on Electronic Structure in LSM Electrodes: An Operando XAS, RIXS and XES Study. *Journal of The Electrochemical Society* **164**, F3064-F3072, doi:10.1149/2.0091710jes (2017).

35 Lee, H. Y., Cho, W. S., Oh, S. M., Wiemhöfer, H. D. & Göpel, W. Active Reaction Sites for Oxygen Reduction in La0.9Sr0.1MnO3 / YSZ Electrodes. *Journal of The Electrochemical Society* **142**, 2659-2664, doi:10.1149/1.2050070 (1995).

36 Liu, J. *et al.* The Electrochemical Performance of LSM with A-site Non-Stoichiometry under Cathodic Polarization. *ECS Transactions* **78**, 689-699, doi:10.1149/07801.0689ecst (2017).

37 Huber, A.-K. *et al.* In situ study of activation and de-activation of LSM fuel cell cathodes – Electrochemistry and surface analysis of thin-film electrodes. *Journal of Catalysis* **294**, 79-88, doi:10.1016/j.jcat.2012.07.010 (2012).

38 Jiang, S. P. & Love, J. G. Origin of the initial polarization behavior of Sr-doped LaMnO3 for O2 reduction in solid oxide fuel cells. *Solid State Ionics* **138**, 183-190, doi:https://doi.org/10.1016/S0167-2738(00)00806-7 (2001).

39 Rohnke, M., Schaepe, K., Bachmann, A. K., Laenger, M. & Janek, J. In situ ToF-SIMS monitoring of SOFC cathodes – A case study of La0.74Sr0.17Mn1.01O2.9 model electrodes. *Applied Surface Science* **422**, 817-827, doi:https://doi.org/10.1016/j.apsusc.2017.06.085 (2017).

40 Huber, T. M. *et al.* Experimental Design for Voltage Driven Tracer Incorporation and Diffusion Studies on Oxide Thin Film Electrodes. *Journal of The Electrochemical Society* **164**, F809-F814, doi:10.1149/2.0711707jes (2017).

41 Horita, T. *et al.* Active Sites Imaging for Oxygen Reduction at the $La_{0.9}Sr_{0.1}MnO_{3-x}$/Yttria-Stabilized Zirconia Interface by Secondary-Ion Mass Spectrometry. *Journal of The Electrochemical Society* **145**, 3196-3202, doi:10.1149/1.1838786 (1998).

42 Lee, Y.-L. & Morgan, D. Prediction of Surface Oxygen Vacancy Concentrations of (La1-xSrx)MnO3. *ECS Transactions* **25**, 2769-2774, doi:10.1149/1.3205838 (2009).

43 Lee, Y.-L., Kleis, J., Rossmeisl, J. & Morgan, D. \textit{Ab initio} energetics of $\text{La}B{\text{O}}_{3}(001)$ ($B=\text{Mn}$, Fe, Co, and Ni) for solid oxide fuel cell cathodes. *Physical Review B* **80**, 224101, doi:10.1103/PhysRevB.80.224101 (2009).

44 Carrasco, J. *et al.* First-principles calculations of the atomic and electronic structure of F centers in the bulk and on the (001) surface of $\mathrm{Sr}\mathrm{Ti}{\mathrm{O}}_{3}$. *Physical Review B* **73**, 064106, doi:10.1103/PhysRevB.73.064106 (2006).

45 Bishop, S. R., Duncan, K. L. & Wachsman, E. D. Surface and bulk oxygen non-stoichiometry and bulk chemical expansion in gadolinium-doped cerium oxide. *Acta Materialia* **57**, 3596-3605, doi:https://doi.org/10.1016/j.actamat.2009.04.017 (2009).
46 Mullins, D. R. The surface chemistry of cerium oxide. *Surface Science Reports* **70**, 42-85, doi:https://doi.org/10.1016/j.surfrep.2014.12.001 (2015).
47 Bjørheim, T. S., Kuwabara, A., Mohn, C. E. & Norby, T. Defects at the (1 1 0) surface of rutile TiO2 from ab initio calculations. *International Journal of Hydrogen Energy* **37**, 8110-8117, doi:https://doi.org/10.1016/j.ijhydene.2011.12.165 (2012).
48 Tompsett, D. A., Parker, S. C. & Islam, M. S. Rutile (β-)MnO2 Surfaces and Vacancy Formation for High Electrochemical and Catalytic Performance. *Journal of the American Chemical Society* **136**, 1418-1426, doi:10.1021/ja4092962 (2014).
49 Lee, W. & Yildiz, B. Factors that Influence Cation Segregation at the Surfaces of Perovskite Oxides. *ECS Transactions* **57**, 2115-2123 (2013).
50 Tsvetkov, N., Lu, Q., Sun, L., Crumlin, E. J. & Yildiz, B. Improved chemical and electrochemical stability on perovskite oxides by oxidizing cations at the surface. *Nature Materials* **15**, 1010-1016, doi:10.1038/nmat4659 (2016).
51 McIntosh, S., Adler, S. B., Vohs, J. M. & Gorte, R. J. Effect of Polarization on and Implications for Characterization of LSM-YSZ Composite Cathodes. *Electrochemical and Solid-State Letters* **7**, A111, doi:10.1149/1.1667792 (2004).
52 Wang, W. & Jiang, S. A mechanistic study on the activation process of (La, Sr)MnO3 electrodes of solid oxide fuel cells. *Solid State Ionics* **177**, 1361-1369, doi:10.1016/j.ssi.2006.05.022 (2006).
53 Zhu, L. *et al.* Electrochemically Driven Deactivation and Recovery in PrBaCo2 O5+delta Oxygen Electrodes for Reversible Solid Oxide Fuel Cells. *ChemSusChem* **9**, 2443-2450, doi:10.1002/cssc.201600658 (2016).
54 Mutoro, E. *et al.* Reversible Compositional Control of Oxide Surfaces by Electrochemical Potentials. *The Journal of Physical Chemistry Letters* **3**, 40-44, doi:10.1021/jz201523y (2011).
55 Huber, A. K. *et al.* In situ study of electrochemical activation and surface segregation of the SOFC electrode material La0.75Sr0.25Cr0.5Mn0.5O(3+/-delta). *Phys Chem Chem Phys* **14**, 751-758, doi:10.1039/c1cp21743g (2012).
56 Ai, N. *et al.* Suppressed Sr segregation and performance of directly assembled La0.6Sr0.4Co0.2Fe0.8O3-δ oxygen electrode on Y2O3-ZrO2 electrolyte of solid oxide electrolysis cells. *Journal of Power Sources* **384**, 125-135, doi:10.1016/j.jpowsour.2018.02.082 (2018).
57 Liang, M. *et al.* Preparation of LSM–YSZ composite powder for anode of solid oxide electrolysis cell and its activation mechanism. *Journal of Power Sources* **190**, 341-345, doi:10.1016/j.jpowsour.2008.12.132 (2009).
58 la O', G. J., Savinell, R. F. & Shao-Horn, Y. Activity Enhancement of Dense Strontium-Doped Lanthanum Manganite Thin Films under Cathodic Polarization: A Combined AES and XPS Study. *Journal of The Electrochemical Society* **156**, B771, doi:10.1149/1.3116228 (2009).
59 Caillol, N., Pijolat, M. & Siebert, E. Investigation of chemisorbed oxygen, surface segregation and effect of post-treatments on La0.8Sr0.2MnO3 powder and screen-printed layers for solid oxide fuel cell cathodes. *Applied Surface Science* **253**, 4641-4648, doi:10.1016/j.apsusc.2006.10.019 (2007).
60 Jiang, S. P. Development of lanthanum strontium cobalt ferrite perovskite electrodes of solid oxide fuel cells – A review. *International Journal of Hydrogen Energy* **44**, 7448-7493, doi:10.1016/j.ijhydene.2019.01.212 (2019).
61 Tian, Y. *et al.* Cobalt-Free Perovskite Oxide La0.6Sr0.4Fe0.8Ni0.2O3−δ as Active and Robust Oxygen Electrode for Reversible Solid Oxide Cells. *ACS Appl Energy Mater* **2**, 3297-3305, doi:10.1021/acsaem.9b00115 (2019).

62 He, Z. *et al.* Cyclic polarization enhances the operating stability of La0.57Sr0.38Co0.18Fe0.72Nb0.1O3-δ oxygen electrode of reversible solid oxide cells. *Journal of Power Sources* **404**, 73-80, doi:10.1016/j.jpowsour.2018.10.009 (2018).
63 Landolt-Bornstein database; Springer Materials, 2010.
64 NIST Database 71; U.S. Department of Commerce: Washington, DC, 2001, accessed in 2017/2018.
65 Values acquired from the KolXPD spectrum fitting program.
66 Chen, Y. *et al.* Segregated Chemistry and Structure on (001) and (100) Surfaces of (La1–xSrx)2CoO4 Override the Crystal Anisotropy in Oxygen Exchange Kinetics. *Chemistry of Materials* **27**, 5436-5450, doi:10.1021/acs.chemmater.5b02292 (2015).
67 <2017 CSR segregation.pdf>. doi:10.1039/C7CS00120G

10.1039/c7cs00120g.
68 Marrocchelli, D., Perry, N. H. & Bishop, S. R. Understanding chemical expansion in perovskite-structured oxides. *Physical Chemistry Chemical Physics* **17**, 10028-10039, doi:10.1039/c4cp05885b (2015).
69 Lee, Y.-L. & Morgan, D. Ab initio and empirical defect modeling of LaMnO3±δ for solid oxide fuel cell cathodes. *Physical Chemistry Chemical Physics* **14**, 290-302, doi:10.1039/c1cp22380a (2012).
70 Kim D, Bliem R, Hess F, Yildiz B, in preparation, 2019.
71 Saranya, A. M. *et al.* Engineering Mixed Ionic Electronic Conduction in La0.8Sr0.2MnO3+δNanostructures through Fast Grain Boundary Oxygen Diffusivity. *Advanced Energy Materials* **5**, 1500377, doi:10.1002/aenm.201500377 (2015).
72 Huber, T. M., Navickas, E., Friedbacher, G., Hutter, H. & Fleig, J. Apparent Oxygen Uphill Diffusion in La0.8Sr0.2MnO3 Thin Films upon Cathodic Polarization. *ChemElectroChem* **2**, 1487-1494, doi:10.1002/celc.201500167 (2015).
73 Brichzin, V., Fleig, J., Habermeier, H. U., Cristiani, G. & Maier, J. The geometry dependence of the polarization resistance of Sr-doped LaMnO3 microelectrodes on yttria-stabilized zirconia. *Solid State Ionics* **152-153**, 499-507, doi:https://doi.org/10.1016/S0167-2738(02)00379-X (2002).
74 Graves, C., Ebbesen, S. D., Jensen, S. H., Simonsen, S. B. & Mogensen, M. B. Eliminating degradation in solid oxide electrochemical cells by reversible operation. *Nature Materials* **14**, 239-244, doi:10.1038/nmat4165 (2015).
75 Abbate, M. *et al.* Controlled-valence properties ofLa1−xSrxFeO3andLa1−xSrxMnO3studied by soft-x-ray absorption spectroscopy. *Physical Review B* **46**, 4511-4519, doi:10.1103/PhysRevB.46.4511 (1992).
76 Suntivich, J. *et al.* Estimating Hybridization of Transition Metal and Oxygen States in Perovskites from O K-edge X-ray Absorption Spectroscopy. *The Journal of Physical Chemistry C* **118**, 1856-1863, doi:10.1021/jp410644j (2014).
77 Mueller, D. N., Machala, M. L., Bluhm, H. & Chueh, W. C. Redox activity of surface oxygen anions in oxygen-deficient perovskite oxides during electrochemical reactions. *Nature communications* **6**, 6097, doi:10.1038/ncomms7097 (2015).
78 Suntivich, J. *et al.* Design principles for oxygen-reduction activity on perovskite oxide catalysts for fuel cells and metal-air batteries. *Nature Chemistry* **3**, 546-550, doi:10.1038/nchem.1069 (2011).
79 Gilbert, B. *et al.* Multiple Scattering Calculations of Bonding and X-ray Absorption Spectroscopy of Manganese Oxides. *The Journal of Physical Chemistry A* **107**, 2839-2847, doi:10.1021/jp021493s (2003).
80 Nakai, S.-i. *et al.* OxygenKx-ray-absorption near-edge structure of alkaline-earth-metal and 3d-transition-metal oxides. *Physical Review B* **36**, 9241-9246, doi:10.1103/PhysRevB.36.9241 (1987).

81 Liu, J.-Y. *et al.* Rational design of ethanol steam reforming catalyst based on analysis of Ni/La2O3 metal–support interactions. *Catalysis Science & Technology* **6**, 3449-3456, doi:10.1039/c5cy00410a (2016).

82 Mizusaki, J. *et al.* Oxygen nonstoichiometry and defect equilibrium in the perovskite-type oxides La1−xSrxMnO3+d. *Solid State Ionics* **129**, 163-177, doi:https://doi.org/10.1016/S0167-2738(99)00323-9 (2000).

83 Lee, Y. L. & Morgan, D. Ab initio and empirical defect modeling of LaMnO(3+/-delta) for solid oxide fuel cell cathodes. *Phys Chem Chem Phys* **14**, 290-302, doi:10.1039/c1cp22380a (2012).

84 Darvish, S., Sabarou, H., Saxena, S. K. & Zhong, Y. Quantitative Defect Chemistry Analysis and Electronic Conductivity Prediction of La0.8Sr0.2MnO3±δPerovskite. *Journal of The Electrochemical Society* **162**, E134-E140, doi:10.1149/2.0361509jes (2015).

85 Van Roosmalen, J. A. M., Cordfunke, E. H. P., Helmholdt, R. B. & Zandbergen, H. W. The Defect Chemistry of LaMnO3±δ: 2. Structural Aspects of LaMnO3+δ. *Journal of Solid State Chemistry* **110**, 100-105, doi:https://doi.org/10.1006/jssc.1994.1141 (1994).

86 Peña, M. A. & Fierro, J. L. G. Chemical Structures and Performance of Perovskite Oxides. *Chemical Reviews* **101**, 1981-2018, doi:10.1021/cr980129f (2001).